



HAL
open science

Production and excitation of molecules by dissipation of two-dimensional turbulence

Pierre Lesaffre, P Todorov, F. Levrier, V. Valdivia, N. Dzyurkevich, B. Godard, L. N Tram, A. Gusdorf, A. Lehmann, E. Falgarone

► To cite this version:

Pierre Lesaffre, P Todorov, F. Levrier, V. Valdivia, N. Dzyurkevich, et al.. Production and excitation of molecules by dissipation of two-dimensional turbulence. Monthly Notices of the Royal Astronomical Society, 2020, 495 (1), pp.816 - 834. 10.1093/mnras/staa849 . hal-02877726

HAL Id: hal-02877726




<https://hal.sorbonne-universite.fr/hal-02877726v1>

Submitted on 22 Jun 2020

HAL is a multi-disciplinary open access archive for the deposit and dissemination of scientific research documents, whether they are published or not. The documents may come from teaching and research institutions in France or abroad, or from public or private research centers.

L'archive ouverte pluridisciplinaire **HAL**, est destinée au dépôt et à la diffusion de documents scientifiques de niveau recherche, publiés ou non, émanant des établissements d'enseignement et de recherche français ou étrangers, des laboratoires publics ou privés.

Production and excitation of molecules by dissipation of two-dimensional turbulence

P. Lesaffre ¹★, P. Todorov,¹ F. Levrier,¹ V. Valdivia ², N. Dzyurkevich,³ B. Godard,¹ L. N. Tram,^{4,5} A. Gusdorf,¹ A. Lehmann ¹ and E. Falgarone¹

¹Laboratoire de Physique de l'ENS, ENS, Université PSL, CNRS, Sorbonne Université, Université Paris-Diderot, Paris, France

²Laboratoire AIM, Paris-Saclay, CEA/IRFU/Sap - CNRS - Université Paris Diderot, 91191 Gif-sur-Yvette Cedex, France

³Institute for Theoretical Astrophysics (ITA), University of Heidelberg, Albert-Ueberle Str., 69120 Heidelberg, Germany

⁴SOFIA-USRA, NASA Ames Research Center, Ms 232-11, Moffett Field, CA 94035, USA

⁵University of Science and Technology of Hanoi, VAST, 18 Hoang Quoc Viet, Hanoi, Vietnam

Accepted 2020 March 17. Received 2020 March 16; in original form 2019 July 8

ABSTRACT

The interstellar medium (ISM) is typically a hostile environment: cold, dilute and irradiated. Nevertheless, it appears very fertile for molecules. The localized heating resulting from turbulence dissipation is a possible channel to produce and excite molecules. However, large-scale simulations cannot resolve the dissipative scales of the ISM. Here, we present two-dimensional small-scale simulations of decaying hydrodynamic turbulence using the CHEMSE code, with fully resolved viscous dissipation, time-dependent heating, cooling, chemistry and excitation of a few rotational levels of H₂. We show that molecules are produced and excited in the wake of strong dissipation ridges. We carefully identify shocks and we assess their statistics and contribution to the molecular yields and excitation. We find that the formation of molecules is strongly linked to increased density as a result of shock compression and to the opening of endothermic chemical routes because of higher temperatures. We identify a new channel for molecule production via H₂ excitation, illustrated by CH⁺ yields in our simulations. Despite low temperatures and the absence of magnetic fields (favouring CH⁺ production through ion-neutral velocity drifts), the excitation of the first few rotational levels of H₂ shrinks the energy gap to form CH⁺. The present study demonstrates how dissipative chemistry can be modelled by statistical collections of one-dimensional steady-state shocks. Thus, the excitation of higher *J* levels of H₂ is likely to be a direct signature of turbulence dissipation, and an indirect probe for molecule formation. We hope these results will help to bring new tools and ideas for the interpretation of current observations of H₂ rotational lines carried out using the *Stratospheric Observatory for Infrared Astronomy (SOFIA)*, and pave the way for a better understanding of the high-resolution mapping of H₂ emission by future instruments, such as the *James Webb Space Telescope* and the *Space Infrared Telescope for Cosmology and Astrophysics*.

Key words: astrochemistry – diffusion – hydrodynamics – shock waves – ISM: kinematics and dynamics – ISM: molecules.

1 INTRODUCTION

Although the diffuse interstellar medium (ISM) is cold and dilute, it appears to be quite fertile in the production of molecules, even when the formation of molecules needs adverse dissociating radiation or

large temperature thresholds, such as for CH⁺ and SH⁺, to be overcome (see Nehmê et al. 2008; Godard et al. 2012). Besides, the excitation of high levels of the molecules such as H₂ is observed despite the low average temperature of this medium (see Gry et al. 2002; Falgarone et al. 2005; Ingalls et al. 2011). Non-thermal phenomena might help to overcome the formation thresholds for these molecules. For instance, the interstellar radiation field ionizes the medium and opens molecular formation routes through

* E-mail: pierre.lesaffre@ens.fr

hydrogenation of the O^+ cation, provided the ultraviolet (UV) irradiation field is not too strong and that the H_2 molecule remains unhindered. This was investigated in detail by Levrier et al. (2012), who found that, for the standard irradiation field and for the densities around 100 cm^{-3} in the diffuse ISM, their models underpredict the observed line fluxes and column densities of molecules. Molecules are too fragile for the diffuse medium irradiation and additional physical processes are needed to increase their abundances, such as ion-neutral drift (as in C-type shocks; see Flower, Pineau des Forêts & Hartquist 1985), turbulent diffusion (Lesaffre, Gerin & Hennebelle 2007) or turbulent dissipation (Godard, Falgarone & Pineau Des Forêts 2009).

Shock compression leads to larger densities and hence more efficient formation rates. The dissipation of turbulence, even when it is incompressible, can bring the medium to high temperature in sharply localized dissipative structures (Falgarone, Pineau des Forêts & Roueff 1995). Pioneering work by Joulain et al. (1998) and Godard et al. (2009) showed that incompressible dissipation could be effective at producing molecules and reproducing observational trends.

In the present study, we aim to explore dissipative chemistry further. We run a multidimensional numerical experiment that renders some of the complexity of the ISM chemistry while fully resolving the dissipation scale. We attempt to characterize some of the processes that lead from dissipation to new molecules. In particular, we decompose a snapshot of decaying turbulence into individual one-dimensional (1D) steady planar shocks. We then proceed to demonstrate that this collection of shocks allows us to account for most of the dissipation, excitation and molecular content in the simulation. This simplified experiment creates a link between complex dynamics and a statistical collection of 1D steady-state shocks. The 1D steady-state shock models can in the future be improved at will by using more refined chemistry and thermal processes, more appropriate to match observational requests.

Our study is the first to include time-dependent excitation of H_2 in multidimensional hydrodynamics. This allows us to uncover another potential means to favour molecule formation, because of lowered temperature thresholds due to the energy stored in excited H_2 . As a first step, we focus here on a two-dimensional (2D) configuration without magnetic fields. In particular, we do not yet include ambipolar drifts, which are known to favour neutral-ion chemical routes.

In Section 2, we introduce the CHEMSES code and we give details of our numerical set-up. In Section 3, we show the results of the numerical experiment: the effects of turbulent dissipation on the average thermodynamical and chemical state of the gas and its H_2 excitation diagram. In particular, we show how excitation can affect some of the chemistry. In Section 4, we explore in detail the role of shocks in our simulation, and how we can recover some of the results of the previous section with a well-chosen collection of 1D planar shocks. In Section 5, we discuss our conclusions and prospects for the future.

2 NUMERICAL METHOD

2.1 The DUMSES hydrodynamics solver

DUMSES,¹ mainly written by S. Fromang, originates from RAMSES, a magnetohydrodynamics (MHD) code with adaptive mesh

refinement (Teyssier 2002; Fromang, Hennebelle & Teyssier 2006). DUMSES uses the MHD solver of RAMSES on a regular grid (i.e. without the adaptive mesh part). We use Van-Leer slopes to estimate the right and left states of the Riemann solver, for which we approximate the fluxes by the Lax–Friedrich prescription (see Toro 1999). The regular grid makes it much easier to implement new physics in DUMSES, especially dissipation and diffusion terms, which require easy access to neighbouring zones. Therefore, it makes it simpler to quickly explore and validate a variety of new methods.

We added in DUMSES the treatment of dissipative terms (viscous momentum diffusion, thermal diffusion and chemical diffusion) as cell-centred differences, which makes them second-order accurate in space. We bracket the Godunov step with two half dissipation steps, one before and one after, in order to retain the second-order accuracy in time of the original scheme (we summarize the resulting scheme in Section 2.3). A constraint using the minimum of all diffusion times across each cell is added to the usual time-step control. Note that, in the present application, we use the same coefficient for momentum, chemical and thermal diffusion, so these time-scales are all the same. This approximation reflects the fact that all three diffusion mechanisms proceed through molecular collisions, and we assume that the carriers have the same mean mass for all three mechanisms. Likewise, we implement resistivity and validate the dissipative terms using Alfvén waves tests, as described in Lesaffre & Balbus (2007). In particular, we verify the quadratic convergence with respect to both time and space resolution. Chemical diffusion is also tested in simple 1D reaction–diffusion steady-state shock fronts. The current version of the code can accommodate magnetic fields, but the present application does not consider them.

The implementation of viscosity used in this paper assumes constant kinematic viscosity ν rather than constant dynamic viscosity $\mu = \nu\rho$, where ρ is the mass density of the fluid. The latter is appropriate for isothermal gases and assumes that the mean free path scales inversely proportional to ρ . While the former might not be reasonable for the ISM, we believe that as long as the collisional time-scales are smaller than the thermal and chemical time-scales, thermochemistry is not affected. However, our assumption of constant ν assumes that the mean free path is a constant. This ensures more homogeneous dissipation length-scales and helps us foresee the necessary resolution. Besides, the steady-state shock fronts offer an analytical solution in that case (see Appendix A2), which simplifies the shock extraction we use in the analysis of our results. The successful comparison of the steady-state shocks with the analytics provides an extra validation of the viscous term’s implementation (see Appendix A3).

2.2 The Paris–Durham steady-state shock code

The Paris–Durham shock code solves the 1D MHD equations in a steady-state frame. It integrates the dynamical, thermal, excitation state and chemical history of fluid particles as they enter a planar steady-state shock (cf. Flower et al. 1985, 2003; Lesaffre et al. 2013; Flower & Pineau des Forêts 2015). For more than 30 yr, the cooling functions, the chemistry and the grain physics have been refined as the shock models were compared with various observations. The included heating and cooling processes are atomic cooling (such as Lyman α , C^+ , C, O), molecular cooling (H_2 , CO, OH, H_2O), cosmic ray ionization heating and photoelectric heating. Collisional exchanges between gas and grains are also included but the grain temperature is kept constant and is a parameter

¹Or ‘RAMSES for the dummies’.

of the problem (set to 15 K). The Paris–Durham shock code makes use of a highly modular set of chemical reactions including two-body gas phase reactions, photoionization, photodissociation, H₂ formation on grain surfaces, cosmic ray induced ionization, desorption, secondary photon ionization and dissociation, grain sputtering and erosion. The code uses DVODE (Brown, Byrne & Hindmarsh 1989) as its time integration engine. The population of excited levels of H₂ is followed in a time-dependent fashion, coupled to the fluid dynamics, which allows direct predictions for the H₂ line intensities.

2.3 Coupling DUMSES and Paris–Durham

DUMSES can incorporate a number of passive scalars, which are evolved alongside the dynamical variables. We make room for the chemical tracers (a total number of 40 species) and the excited levels of H₂ (seven levels), which will be taken care of by the Paris–Durham code: a total of 47 scalars on top of the four dynamical variables (density ρ , total energy E and the two components of the velocity). We interfaced Paris–Durham to compute only the isochoric time evolution of a single gas temperature, chemical abundances and excited levels population of H₂. The time evolution of internal energy and scalars (‘thermochemistry’) is delegated to Paris–Durham at each time-step for each zone of the simulation. The irradiation conditions are assumed to be uniform, which sets a maximum extension for the computational box; the visual extinction across the box should not exceed about 0.01 mag.

We use the seven lowest levels of H₂ up to a transition energy of 3474 K, close to the energy threshold for CH⁺ formation (see Section 3.4.5). The largest rotational number $J_{\max} = 6$ is indeed chosen to target the energy gap for the CH⁺ formation: this was also adopted in early C-type shock studies by Flower & Pineau des Forets (1998). We have also checked, for a 1D steady-state shock at 2 km s⁻¹, that $J_{\max} = 6$ is sufficient to give converged temperature and H₂ excitation profiles compared to $J_{\max} = 150$. However, we note that the chemical profile of CH⁺ in this shock is very slow to converge with respect to J_{\max} , with its maximum abundance enhanced by a factor of 2 between $J_{\max} = 6$ and $J_{\max} = 150$ (see Section 3.4.5).

We adopt the same minimal network of 32 gas species as in Lesaffre et al. (2004a), necessary to model the abundance of the cooling agents of the ISM: H, C⁺, C, O, H₂, CO, OH and H₂O. It is complemented by eight variables necessary to model grain cores and their mantles, as in Flower et al. (2003), which brings the total number of chemical variables to 40. The resulting network consists of 172 reactions. As in Lesaffre et al. (2013), the computation of the rate of the ion-neutral reaction C⁺ + H₂ → CH⁺ + H takes advantage of the state by state description of the H₂ populations and we follow the prescription of Gerlich, Disch & Scherbarth (1987), as advocated in Agúndez et al. (2010).

In order to retain second-order accuracy in time for the whole time-step, we split thermochemistry and hydrodynamics by starting with half a time-step for thermochemistry, followed by one full hydrodynamical step, and then half a thermochemical step. To retain the necessary symmetry required by second-order time-integration, we placed the two half-steps for the dissipation processes wrapped around this hybrid hydrodynamical and thermochemical time-step. Thus, the final ordering of the time-step is as follows:

(i) half a dissipation step (momentum, chemical and thermal diffusion);

- (ii) half a thermo-chemical step (isochoric evolution of pressure, chemical species and H₂ populations);
- (iii) one hydrodynamical step (classic Godunov step);
- (iv) half a thermo-chemical step;
- (v) half a dissipation and diffusion step.

Thermochemistry can potentially affect the dynamics. For example, ionization or dissociation increases the total number of particles, and hence the pressure. The time-step control should reflect this constraint. We record the relative pressure variation during each thermochemical step. If the relative pressure change due to thermochemistry is larger than 5 per cent, we reduce the following time-step to satisfy the constraint. Otherwise, we use the minimum between the diffusive and Courant–Friedrichs–Lewy (CFL) conditions. We multiply the resulting time by 0.7 and set it to the next time-step for more safety. In our applications, the most stringent constraint is usually given by the CFL condition, so we effectively function at a Courant number (i.e. the ratio between the time-step and the CFL maximum stable time step) of 0.7.

As noted by several authors (Plewa & Müller 1999; Glover et al. 2010), non-linear evolution and advection of the set of chemical species does not retain constant elemental composition. In particular, Glover et al. (2010) designed a scheme called the modified consistent multifluid advection (MCMA) to recover multiple elemental conservation constraints in a set of species. We extend this method to the H₂ level populations such that the sum of the populations of excited H₂ levels has to match the H₂ number density. We apply it to the vector of chemical scalars after each thermochemical step, and on the Godunov fluxes of the chemical scalars, before they are advected.

The DVODE solver for the whole set of thermochemical variables is CPU-intensive. For each pixel, we evaluate the initial thermochemical time-scale at the beginning of each thermochemical step by computing the shortest evolution time-scale between all scalars and the temperature. We decide to resort to DVODE only if this evolution time-scale is shorter than 10 times the hydrodynamical step (i.e. when the thermochemical evolution is stiff). Otherwise, the evolution for this pixel is slow enough that we can use a much faster Runge–Kutta method of order 2 without loss of accuracy. This saves a considerable amount of CPU time, as a significant fraction of the simulation volume has slow thermochemical evolution.

To further reduce CPU consumption, we switch all atomic coolants off except for the C⁺ ion, which often dominates cooling in the conditions of diffuse ISM (see fig. 3b of Wolfire et al. 1995, for instance). In particular, we switch off atomic O cooling, although we know it can be important in low velocity shocks (see Lesaffre et al. 2013). This means that the temperature in the cooling layers of the shocks is slightly overestimated, which results in slightly longer relaxation scales behind the adiabatic fronts (by 30 per cent on a shock of about 2 km s⁻¹). For a fair comparison, we retain this approximation in both the multidimensional runs and in the steady-state runs of the Paris–Durham code. Indeed, the main purpose of the present study is to demonstrate the role of shocks in multidimensional turbulent dissipation. Future work on 1D steady-state shocks can strive to refine the observationally relevant microphysics.

We refer to the resulting code as CHEMSES, which thus joins the group of multidimensional codes that couple MHD and chemistry, such as ASTROBEAR (Poludnenko, Frank & Blackman 2002), PLUTO (Mignone et al. 2007), KROME (Grassi et al. 2014) and NIRVANA (Ziegler 2005, 2018). Our code is one of the few that control

the dissipation and diffusion physics exactly. To our knowledge, it is the only code that considers the time dependence of the H_2 level populations. The way we interfaced DUMSES with Paris–Durham makes it easy to validate CHEMSES against steady-state shock code computation (see Appendix A1). To our knowledge, this is the first existing test of the coupling between hydrodynamics and thermochemistry. Previously existing codes usually performed only pure advection tests, which do not test the whole extent of the interplay between chemistry, thermal evolution and dynamics.

2.4 Simulation parameters

2.4.1 Length-scales and resolution

Our objective is to test whether turbulence dissipation can potentially produce molecules and excite them even in a diffuse, moderately shielded medium. Levrier et al. (2012) have shown that photon-dominated region (PDR) model predictions for CO column densities fall short of a factor of 10 for lines of sight where $N(\text{H}_2)$ is around a few 10^{20} cm^{-2} (see their fig. 11, for example), typical of the diffuse ISM. These diffuse ISM conditions correspond to a density around $n_{\text{H}} = 100 \text{ cm}^{-3}$, which we adopt as our average density. For molecular gas and 10 per cent He in number, this translates to a total number density of particles of $n_{\text{tot}} = 60 \text{ cm}^{-3}$.

For this density, the elastic collision mean free path is of the order of $\lambda_{\text{MFP}} \sim 10^{15} \text{ cm}^{-2}/n_{\text{tot}} \sim 1.7 \times 10^{13} \text{ cm}$ (see Monchick & Schaefer 1980). Given the typical adiabatic sound speed in this diffuse medium (about $c_s = \sqrt{\gamma p/\rho} \sim 0.8 \text{ km s}^{-1}$ at a temperature around 100 K), this sets the viscous coefficient to a value around $\nu \sim c_s \lambda_{\text{MFP}} \sim 10^{18} \text{ cm}^2 \text{ s}^{-1}$. The other diffusive coefficients (chemical and thermal) are also set to this value (see Section 2.1).

We focus our study on one periodic simulation box of decaying 2D turbulence. We can thus afford a domain size of $N = 1024$ pixels aside for a total CPU time of about 100 000 h during six initial turnover time-scales ($t_{\text{turnover}} = L/u_{\text{rms}}$; see Table 1). Convergence studies for both the viscous term (see Appendix A3) and the chemical term point towards a resolution such that $L \sim N\nu/\Delta u$, where Δu is the typical shock speed jump (which we take as $\Delta u \sim 1 \text{ km s}^{-1}$). Therefore, we limit the physical size of our domain to $L = 10^{16} \text{ cm}$. This is more than three orders of magnitude smaller than typical sizes of diffuse clouds, but it is the price to pay in order to resolve the dissipation scale of the diffuse ISM (100 au) in our simulation.

2.4.2 Irradiation conditions

The irradiation conditions are those of the diffuse ISM: standard stellar irradiation field (ISRF; Draine 1978) mildly shielded by an external buffer of visual extinction thickness $A_{\text{V}0} = 0.1 \text{ mag}$, free of CO but with a column density of 10^{20} cm^{-2} of H_2 molecules which provides strong self-shielding to the dissociation of molecular hydrogen (see Lesaffre et al. 2013). This medium is thus expected to contain H_2 , but be deprived of other molecules. For historical reasons, the cosmic ray ionization rate was set to a value $\zeta = 3 \times 10^{-17} \text{ s}^{-1}$; this is now about 10 times lower than the currently accepted standard rate at these H_2 column densities (see Indriolo, Fields & McCall 2015; Neufeld & Wolfire 2017, fig. 6). This may change the H_3^+ chemistry essentially in such a way that its abundance will be proportional to ζ (see Section 3.4.2). However, it will presumably not affect the comparison between our simulations

Table 1. Physical parameters of the simulation.

Parameter	Value
Average density	$n_{\text{H}} = 100 \text{ cm}^{-3}$
Domain size	$L = 10^{16} \text{ cm}$
Resolution	1024^2 pixels
Pixel size	$9.7 \times 10^{12} \text{ cm}$
Temperature at $t = 0$	$T_0 = 66 \text{ K}$
Adiabatic sound speed at $t = 0$	$c_{\text{s}0} = 0.67 \text{ km s}^{-1}$
rms velocity at $t = 0$	$u_{\text{rms}} = 2.1 \text{ km s}^{-1}$
rms initial Mach number	$u_{\text{rms}}/c_{\text{s}0} = 3.1$
Initial turnover time-scale	1500 yr
Total duration of the simulation	10 000 yr
Reynolds number at $t = 0$	$Re = Lu_{\text{rms}}/\nu = 2100$
UV irradiation field (Draine’s units)	$G_0 = 1$
Visual extinction	$A_{\text{V}} = 0.1 \text{ mag}$

and the molecular yields by 1D planar shocks (see Section 4), provided the same value of ζ is used in both cases.

2.4.3 Initial composition

Elemental composition is similar to that used in Lesaffre et al. (2013). The H_2 levels are initialized with separate Boltzmann equilibria for ortho levels, on the one hand, and para levels, on the other hand. We pre-initiate the ortho-to-para ratio to the value of 3 and we integrate chemistry, H_2 excitation and thermal evolution during 10^7 yr from atomic conditions. This provides a first guess near chemical and thermal equilibrium as initial conditions for our hydrodynamic run. During the time interval of pre-initial conditions, the ortho-to-para ratio drops from 3 to a minimum of 0.2 after 6×10^5 yr before slowly rising towards its equilibrium value of 1.5. At the end of the pre-initialization time of 10^7 yr, the ortho-to-para ratio has reached the value of 0.67, which is hence adopted at the beginning of the 2D simulation.

2.4.4 Initial velocity field

We seed turbulence with an initial random solenoidal velocity field. Fourier modes have random phase and uniform amplitude between wavenumber k_0 and $5k_0$ in units of the fundamental mode of the box ($k_0 = 2\pi/L$). As a result, the initial power spectrum (proportional to k times the amplitude of modes in a 2D geometry) peaks at $5k_0$.

We then scale the initial absolute amplitude for the velocity field such that its root mean square (rms) is $u_{\text{rms}} = 2.1 \text{ km s}^{-1}$. Our experiment describes a very small region as if it had just flown through a much larger scale dissipative structure. It gets a sudden kick and we observe it during a few thousand yr as it relaxes back to a quiescent state close to the initial conditions. We stop the simulation at a time $t = 10^4$ yr, which corresponds to slightly more than six initial turnover times Lu_{rms} (see Table 1 for a summary of the main physical parameters). Note that the rms velocity averaged over the whole duration of the simulation is 0.5 km s^{-1} , consistent with the higher end of rms velocity observations at a length-scale of $L = 10^{16} \text{ cm}$ (see fig. 6 in Falgarone, Hily-Blant & Pety 2009). We also tested a two times lower initial rms velocity (see Section 4.5).

3 RESULTS

3.1 Average behaviour

Fig. 1 displays the evolution of the volume-averaged, maximum

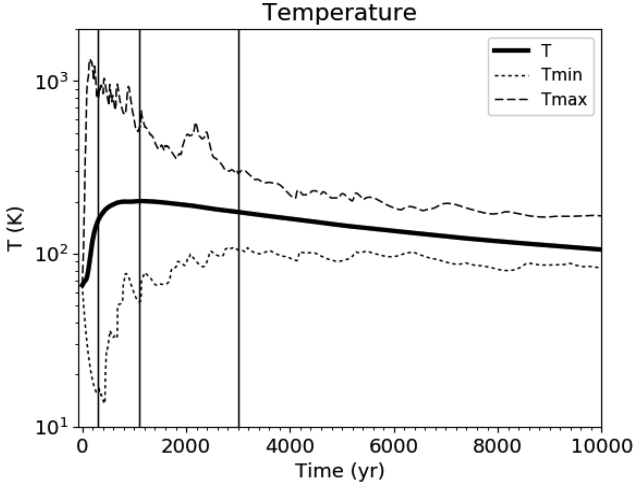


Figure 1. Time evolution of the volume-averaged temperature (solid line). The minimum and maximum values of the temperature are shown as dotted and dashed lines, respectively. Thin vertical lines mark three epochs of reference: I at $t = 300$ yr, II at $t = 1100$ yr and III at $t = 3000$ yr.

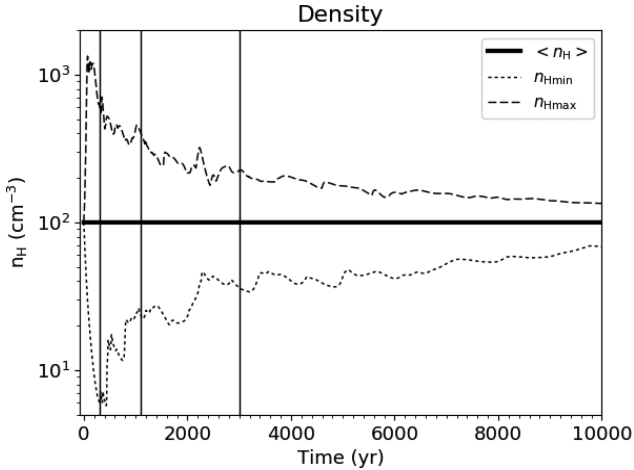


Figure 2. Time evolution of the averaged density (solid line). The minimum and maximum values of the density are shown as dotted and dashed lines, respectively. Reference times are indicated as in Fig. 1.

and minimum temperature during the simulation. The maximum temperature has a very sudden surge to 1350 K at $t = 150$ yr when the first shock fronts are fully formed. Its jagged evolution hints at new shock fronts forming (e.g. when two shocks collide), whose strength overtakes previous shocks, which cool down and damp away. Because the total mass is conserved, initial compression in shocks must be balanced by diluted areas where the gas undergoes dilatational cooling – hence, the initial dip in the minimum temperature. The average temperature reaches a mild maximum at 200 K where it stays between time $t = 500$ yr and $t = 1500$ yr before it slowly decreases again towards the initial temperature 66 K. The final evolution is milder and the temperature spans only about a factor of 2 between its minimum and maximum values.

Fig. 2 displays the evolution of the averaged density, which is perfectly uniform as the code is conservative. The maximum density reflects the shock compression while the minimum density reflects the compensating dilatation regions.

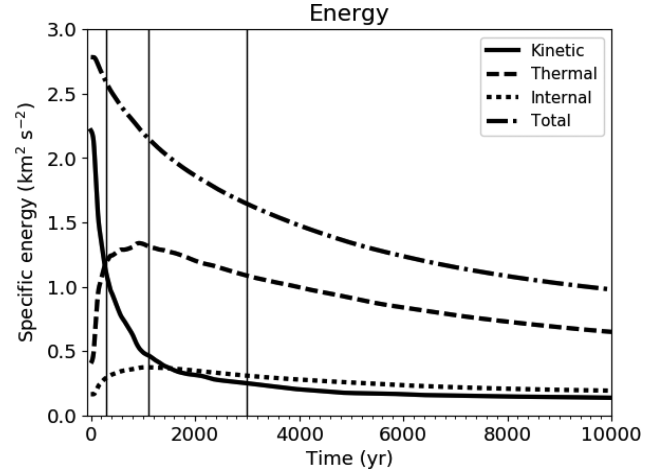


Figure 3. Time evolution of averaged specific energies: kinetic (solid line), thermal (dashed line), internal (excitation energy of H_2 , dotted line) and the sum of all three (dash-dotted line). Values are expressed in $\text{km}^2 \text{s}^{-2}$. Reference times are indicated as in Fig. 1.

3.1.1 Energetics

Fig. 3 displays the evolution of three components of the total specific energy:

(i) the kinetic energy $E_{\text{kin}} = \langle (1/2)\rho u^2 \rangle / \langle \rho \rangle$, where ρ is the mass density, u is the magnitude of the velocity and angular brackets denote an average over the computational domain;

(ii) the thermal energy $E_{\text{th}} = (3/2) \langle p \rangle / \langle \rho \rangle$ where p is the thermal pressure;

(iii) the internal energy, carried by the excitation of H_2 molecules: $E_{\text{int}} = \sum_{J=1}^{J=6} \langle n_J(H_2) \rangle E_J / \langle \rho \rangle$, where $n_J(H_2)$ is the number density of H_2 molecules in the J th excited level (with vibrational number $v = 0$ and rotational number J) and E_J is the energy of this level above ground state (we adopt the convention $E_0 = 0$).

Thermal versus kinetic energy equipartition is reached very early at $t = 270$ yr. Kinetic energy then decays very quickly, but energy is stored in thermal and internal components for a much longer time before it is radiated away.

The evolution of kinetic energy is determined by dissipative and compressive heating (Fig. 4) and expressed by

$$-\left\langle \frac{\partial E_{\text{kin}}}{\partial t} \right\rangle = -\langle p \nabla \cdot \mathbf{u} \rangle + \langle \epsilon_{\text{viscous}} \rangle + \langle \epsilon_{\text{numerics}} \rangle. \quad (1)$$

Here, we explicitly separate the total dissipation ϵ into a physical term described by

$$\epsilon_{\text{viscous}} = \rho \nu \partial_i u_j \left[\frac{1}{2} (\partial_i u_j + \partial_j u_i) - \frac{1}{3} \nabla \cdot \mathbf{u} \delta_{ij} \right], \quad (2)$$

and a numerical term $\epsilon_{\text{numerics}}$ due to the truncation of the scheme. The perfect agreement between the open circles ($-\langle p \nabla \cdot \mathbf{u} \rangle + \langle \epsilon_{\text{viscous}} \rangle$) and the solid line ($-\langle \partial E_{\text{kin}} / \partial t \rangle$) in Fig. 4 illustrates the fact that $\langle \epsilon_{\text{numerics}} \rangle$ is very small (of the order of a few per cent at most compared with the total rate of variation of the kinetic energy): dissipation processes are, on average, very well resolved. The evolution of the total dissipation is smoother than the kinetic energy rate of decrease, which varies rapidly because of the fluctuating compressive heating.

The temperature evolution is sensitive to the dissipative heating as well as to a number of radiative cooling and photoelectric and cosmic ray heating processes. The radiative cooling from H_2 can be

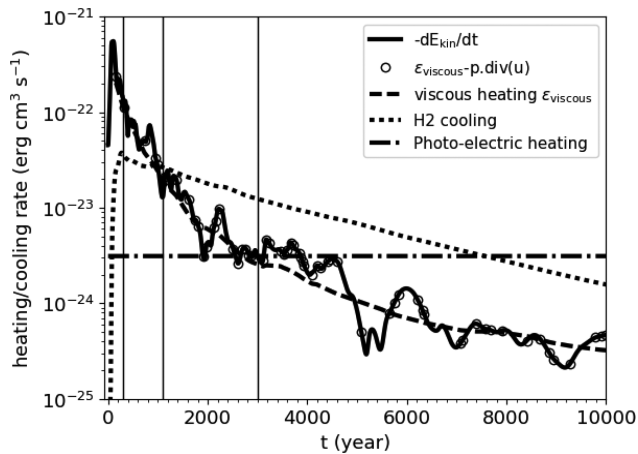


Figure 4. Time evolution of some heating and cooling rates. The viscous heating is computed only at times for which the maps of all relevant variables (ρ , u , p) were retained. The kinetic energy decrease rate is computed from finite difference on the kinetic energy data of Fig. 3 (solid line) or from individual snapshots where the dissipative heating and compressive heating are integrated over the computational box and added together (open circles). The photoelectric heating rate (dash-dotted line) and the cooling from spontaneous de-excitation from H_2 levels (dotted) are also indicated. Reference times are indicated as in Fig. 1.

estimated from the average populations of the H_2 levels,

$$\langle \Lambda_{\text{H}_2} \rangle = \sum_{J=2}^{J=6} A_J \langle n_J(\text{H}_2) \rangle E_J, \quad (3)$$

where A_J is the Einstein de-excitation coefficient of the J th rotational level. Fig. 4 shows that although H_2 cooling reacts immediately to the initial conditions, it takes a long time to relax back to its original value. The rate of photoelectric heating is $\Gamma_{\text{photoel}} = 4 \times 10^{-26} n_{\text{H}} \exp(-2.5A_{v0}) \text{ erg cm}^{-3} \text{ s}^{-1}$ (Black & van Dishoeck 1987). Because the visual extinction $A_{v0} = 0.1$ mag is assumed to be a uniform constant and mass is conserved, the average photoelectric heating rate is constant over time. Although this heating rate begins to dominate over the average dissipative heating at around $t = 3000$ yr, the average temperature at this point, and even beyond, is still significantly above its initial radiative equilibrium (see Fig. 1). This is a manifestation of the intermittency of the dissipative rate, which peaks at values much larger than its average, and of the thermal inertia of the gas, which takes time to cool down after a burst of heating.

3.1.2 Average abundances

Fig. 5 shows the time evolution of the average abundances of selected molecules. Molecular chemistry is clearly boosted for a significant amount of time, and it then decays back to the initial chemical equilibrium. For example, the abundance of CO is enhanced by a factor of 10 and survives during a few thousand yr after the initial kinetic energy burst. By contrast, the abundance of the H_3^+ cation is enhanced by a factor of 2. In Section 3.4.2, we discuss possible mechanisms that can enhance molecular production.

3.1.3 H_2 excitation

Fig. 5 also shows that the upper-level population of the $\text{H}_2\text{O}-\text{OS}(1)$ transition is boosted by a factor of nearly 2000, in conjunction with

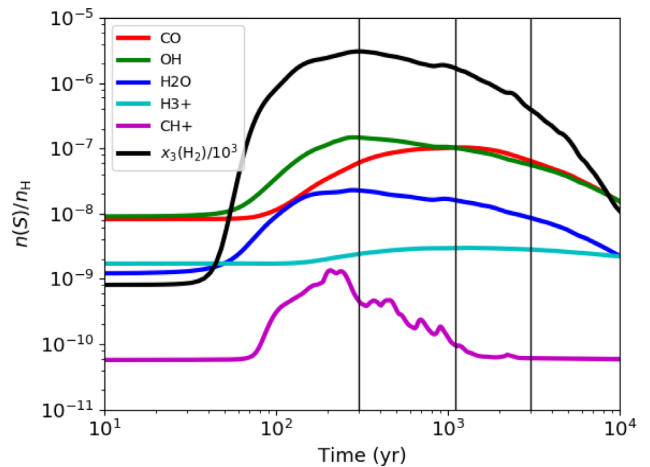


Figure 5. Time evolution of the average abundance relative to n_{H} for some relevant species. Also indicated is the population of the level $v = 0$, $J = 3$ of H_2 , scaled down by a factor of 1000 to help readability. Reference times are indicated as in Fig. 1 (note that the time axis is now logarithmically scaled).

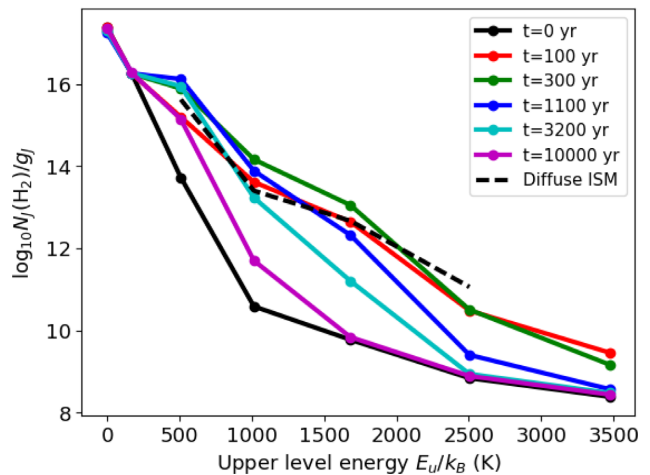


Figure 6. Box-averaged H_2 excitation diagrams at various epochs, showing $\log_{10} N_J/g_J$, where N_J is the total column density (in cm^{-2}) of level J across the box and g_J is its statistical weight. The black dashed line shows numbers for a line of sight through the galaxy, as observed by Falgarone et al. (2005). Column densities are taken from their table 2, divided by a factor of 10^4 to account for the fact that their line of sight has a total column density of the order of $N_{\text{H}} = 10^{22} \text{ cm}^{-2}$ while our simulation only has $N_{\text{H}} = 10^{18} \text{ cm}^{-2}$.

the chemical yields, which illustrates one possible observational signature of turbulent dissipation. Fig. 6 shows the evolution of the H_2 excitation diagram averaged over the computational domain. H_2 levels above $J = 3$ are quickly excited and reach a maximum between $t = 200$ yr and $t = 300$ yr, depending on which level is considered, shortly after the maximum of the temperature (see Fig. 1). However, level $J = 2$ reaches its maximum around $t = 1000$ yr. Excited populations are maintained, despite the fact that the average temperature decreases again to values close to the initial state. The excitation of the lowest energy levels decays slower than for higher energy levels, in agreement with the increase of Einstein coefficients with the energy of the level: indeed, $1/A_{ij} = 1000$ yr for $J = 2$ while its value is 1 yr for $J = 6$. The slow variation of H_2 excitation justifies the use of a time-dependent treatment for populations of its excited levels. The ortho-to-para ratio is virtually

constant throughout the simulation (its value is about 0.67 initially and increases to 0.71 at the end of the simulation).

The black dashed line in Fig. 6 shows observational results from Falgarone et al. (2005) for a line of sight throughout our Galaxy selected to intercept mainly diffuse gas. We scale down the observed column densities by a factor of 10^4 to account for the reduced total column density in our simulation ($N_{\text{H}} = 10^{18} \text{ cm}^{-2}$ across our simulation, while it is estimated to be of the order of 10^{22} cm^{-2} in the observed line of sight). Both the absolute value and the slope of the resulting excitation diagram appear roughly consistent with the early stages of the simulation, between $t = 100 \text{ yr}$ and $t = 300 \text{ yr}$. The slope in the observations is slightly shallower than in our simulations, hinting at the presence of gas with even larger temperatures in the line of sight. Current and future observations by the *Stratospheric Observatory for Infrared Astronomy (SOFIA)*, the *James Webb Space Telescope (JWST)* and the *Space Infrared Telescope for Cosmology and Astrophysics (SPICA)* will require and allow more precise and detailed comparisons.

3.2 Velocity field

In three-dimensional (3D) compressible experiments of solenoidal driving for turbulence, it is customary to show the spectra of $\rho^{1/3}\mathbf{u}$, rather than those of kinetic energy (ρu^2) or velocity (\mathbf{u}), because they exhibit Kolmogorov-like ($k^{-5/3}$) scaling (Federrath 2013). Fig. 7 shows spectra of $\rho^{1/3}\mathbf{u}$ for three selected times of the simulation. Energy always decreases with time. These spectra display a power-law behaviour for about a decade, close to k^{-3} , but their slope slowly drifts to steeper values as time proceeds. These power laws experience an exponential cut-off at small scales due to viscous dissipation and the cut-off scale appears to grow with time. We computed the cross-scale flux $\Pi(k)$ as in Grete et al. (2017), which positive sign indicates that the net cascade of kinetic energy is direct, from large to small scales (see Fig. 7). We followed Grete et al. (2017) to decompose this energy flux across scales according to the sum of three different physical contributions. The energy flux due to advection \mathcal{T}_{UUa} (defined in Grete et al. 2017, equation 25) is positive, while the fluxes due to compression \mathcal{T}_{UUc} (see Grete et al. 2017, equation 25) and pressure terms \mathcal{T}_{PU} (see Grete et al. 2017, equation 32) are negative.

3.3 Dissipation field

We study the dissipation term $\epsilon_{\text{viscous}}$. When $\mu = \rho\nu$ is a uniform constant, we can write

$$\langle \epsilon_{\text{viscous}} \rangle = \langle \epsilon_{\text{comp}} + \epsilon_{\text{sol}} \rangle, \quad (4)$$

where the compressive dissipation is

$$\epsilon_{\text{comp}} = \frac{4}{3} \rho \nu (\nabla \cdot \mathbf{u})^2 \quad (5)$$

and the vortical (or solenoidal) dissipation is

$$\epsilon_{\text{sol}} = \rho \nu (\nabla \cdot \mathbf{u})^2. \quad (6)$$

However, equality (4) only holds averaged over the computational domain, and we use ν as a uniform constant, not μ . This means, in our case, that the quantity $\epsilon_{\text{defect}} \equiv \epsilon_{\text{viscous}} - \epsilon_{\text{comp}} - \epsilon_{\text{sol}}$ can be non-zero both locally and globally. Nevertheless, Fig. 8 shows that ϵ_{defect} generally remains small: this colour map shows essentially blue (ϵ_{comp}) and green (ϵ_{sol}), almost no red ($|\epsilon_{\text{defect}}|$), and the global average of $|\epsilon_{\text{defect}}|$ amounts to less than 10 per cent of the total dissipation rate at worst. The same figure shows that compressive

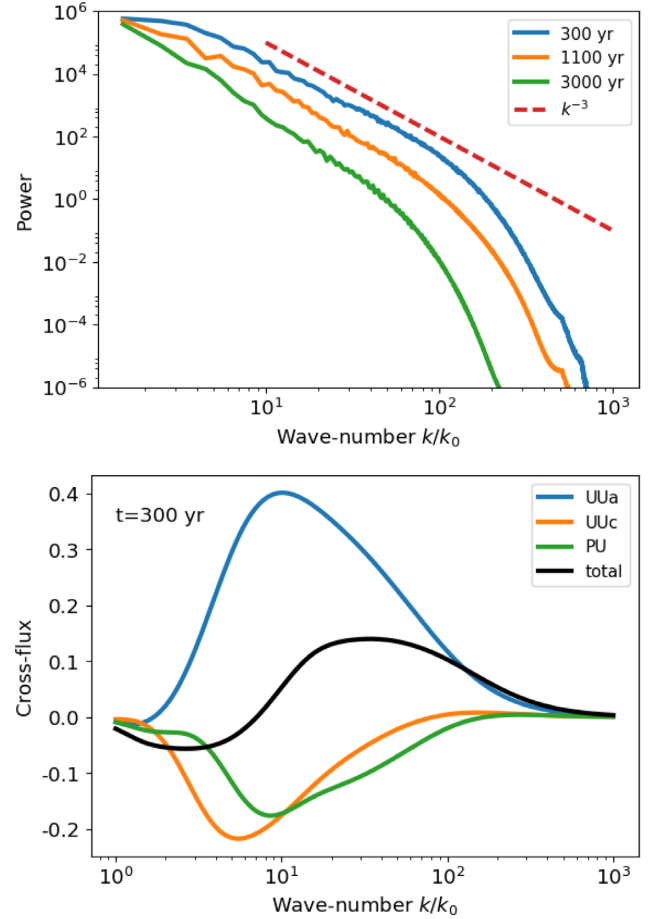


Figure 7. Top: time evolution of the spectra of $\rho^{1/3}\mathbf{u}$ (dimensionless units). Bottom: energy flux across wavelength k : $\Pi(k) = \mathcal{T}_{UUa} + \mathcal{T}_{UUc} + \mathcal{T}_{PU}$ (black) and its components (blue, advection \mathcal{T}_{UUa} ; yellow, compression \mathcal{T}_{UUc} ; green, pressure \mathcal{T}_{PU} ; see text and Grete et al. 2017) at $t = 300 \text{ yr}$.

dissipation occurs in ridges with slightly fewer than 10 pixels ($\sim 6 \text{ au}$) of width, while vortical dissipation trails these compressive fronts.

Indeed, vorticity is known to be generated at shock crossings or at strong shock-front bends. The compressive heating fraction strongly decreases over time: from 80 per cent at the beginning to about 8 per cent at the end of the simulation (not shown here). The statistics of viscous dissipation roughly display a lognormal behaviour (see Fig. 9), which is a signature of its intermittency (Kolmogorov 1962).

3.4 Spatial distributions

3.4.1 Temperature and density

Heating and compression in the wake of strong dissipation regions hint at shocks (see Fig. 10). An inspection by eye of the pressure field frame by frame (one frame every 10^9 s , or about 30 yr) reveals the shocks as pressure steps and allows us to witness their progression (see Fig. 11). Shocks are already formed from the second frame and they appear in pairs, back to back. Around $t = 200 \text{ yr}$, the first shock crossings occur, and start generating secondary shocks and trailing vorticity.

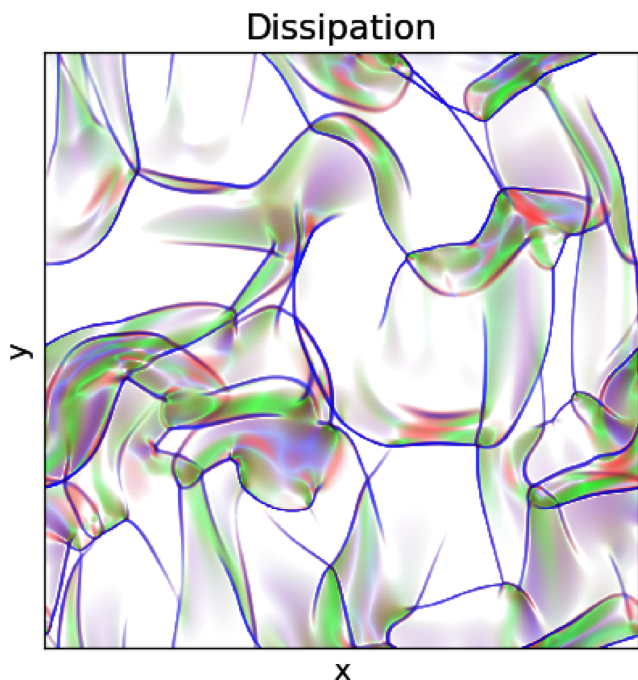


Figure 8. Map of the different components of the dissipation heating near the peak of dissipation at $t = 300$ yr. The RGB colours of each pixel are proportional to: blue, compressive heating ϵ_{comp} ; green, solenoidal heating ϵ_{sol} ; red, remainder $|\epsilon_{\text{defect}}|$; while the intensity is proportional to the logarithm of their sum. The pixels of lowest dissipation are masked out (under a threshold such that their total dissipation amounts to 3 per cent of the total dissipation).

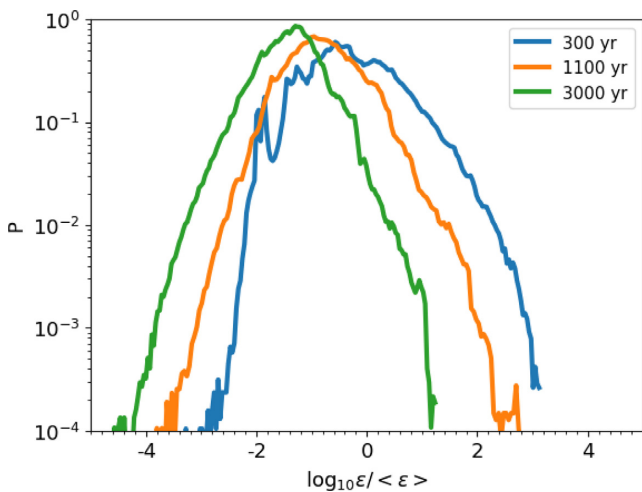


Figure 9. Probability distribution function of the viscous dissipation $\epsilon_{\text{viscous}}$ at three selected epochs.

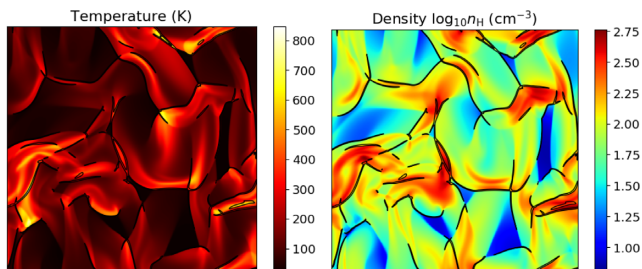


Figure 10. Temperature (left panel, linear scale) and density (right panel, log scale) maps at $t = 300$ yr. Thin black contours of strong dissipation (mean plus two standard deviations of $\log \epsilon$) are overlaid to guide the eye.

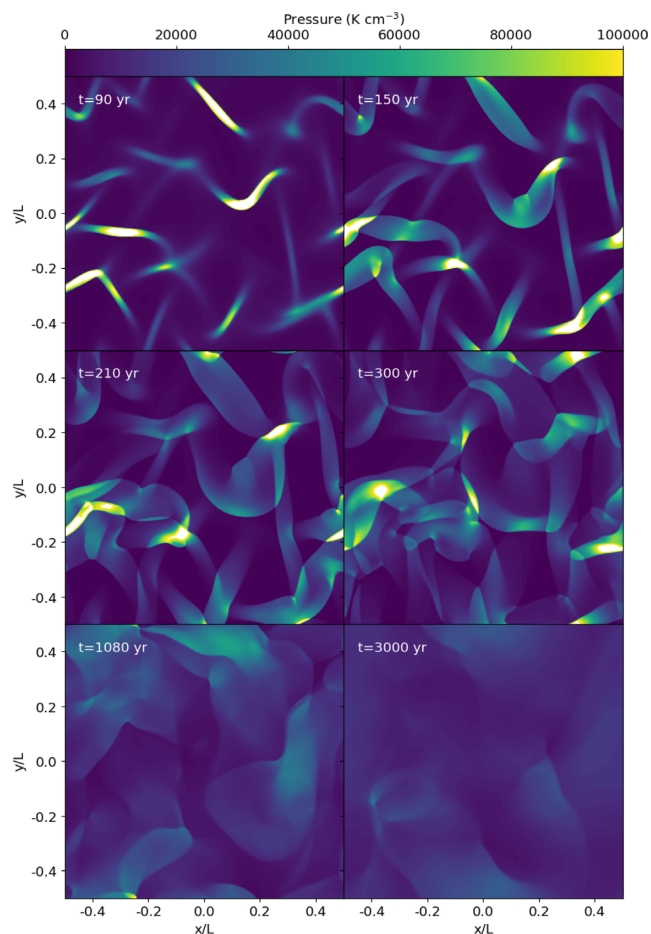


Figure 11. Snapshots of pressure maps in the simulation at selected times.

3.4.2 Chemical analysis

We saw in Section 3.1.2 that the abundance of the H_3^+ cation is only mildly enhanced throughout our numerical experiment. Indeed, its chemistry results from the balance between cosmic ray ionization and dissociative recombination: its abundance is insensitive to density, and mildly favoured by temperature increase through the $1/\sqrt{T}$ dependence of the recombination rate of H_3^+ . If we write the balance between recombination and hydrogen cosmic ray ionization, we can estimate its abundance as

$$n(\text{H}_3^+) = \frac{\zeta}{R_0} \frac{x(\text{H}_2)}{x(\text{C}^+)} \left(\frac{T}{300 \text{ K}} \right)^{0.5}, \quad (7)$$

where $R_0 = 1.5 \times 10^{-7} \text{ cm}^{-3} \text{ s}^{-1}$ is the H_3^+ recombination rate at $T = 300 \text{ K}$. We define $n(S)$ as the abundance and $x(S) = n(S)/n_{\text{H}}$ as the relative abundance of species S , and we have assumed that the ionization degree is given by the abundance of C^+ , the main carrier of charges here. The relative abundance of H_2 is quite uniform, and equal to $x(\text{H}_2) = 0.4$. In our simulations, the correlation between the abundance of the H_3^+ cation and the temperature is remarkable and displays the expected scaling in \sqrt{T} (see Fig. 12, top-left panel). The constant ratio of 70 per cent between the simulation results and the dashed line still eludes us.

The temperature in this simulation is not large enough to overcome the temperature activation barrier of 3000 K of the hydrogenation reaction $\text{H}_2 + \text{O} \rightarrow \text{OH} + \text{H}$, as in the shocks of Lesaffre et al.

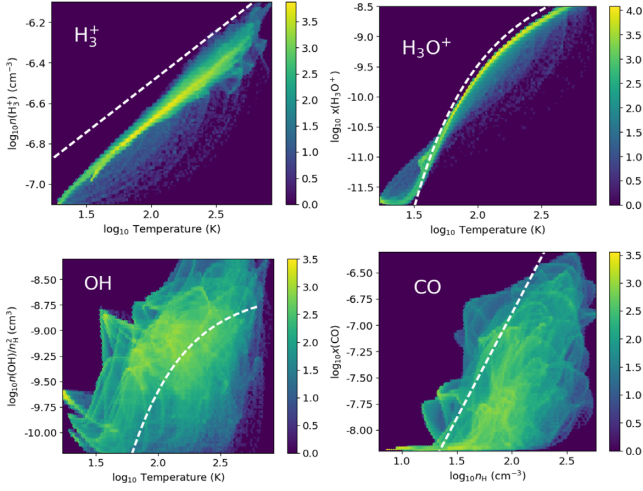


Figure 12. Joint distribution between various abundances and temperature or density with predictions from chemical balance (white dashed lines) for H_3^+ at top left (equation 7), H_3O^+ at top right (equation 8), OH at bottom left (equation 9) and CO at bottom right (equation 10, without the exponential temperature dependence). The colour scale indicates the decimal logarithm of the number of pixels in the simulation that fall in each hexagonal bin. These distributions are shown for time $t = 300$ yr.

(2013). However, it helps to trigger the charge exchange reaction $\text{H}^+ + \text{O} \rightarrow \text{O}^+ + \text{H}$, which has a much milder threshold of 227 K. The hydrogenation reaction chain can then proceed from O^+ until H_3O^+ , which recombines to give either H_2O (branching 1/3) or OH (branching 2/3). The hydrogenation chain is so efficient that the relative abundance of H_3O^+ can be obtained quite accurately from the balance between the rate of $\text{H}^+ + \text{O} \rightarrow \text{O}^+ + \text{H}$ with rate $R_1 = 6 \times 10^{-10} e^{-227\text{K}/T} \text{ cm}^3 \text{ s}^{-1}$ and the rate of recombination of H_3O^+ with rate $R_2 = 1.2 \times 10^{-6} (T/300 \text{ K})^{-0.5} \text{ cm}^3 \text{ s}^{-1}$,

$$x(\text{H}_3\text{O}^+) = 5 \times 10^{-4} \frac{x(\text{O})x(\text{H}^+)}{x(\text{C}^+)} (T/300 \text{ K})^{0.5} e^{-227\text{K}/T}, \quad (8)$$

as illustrated by Fig. 12 (top-right panel). The abundances relative to n_{H} of atomic O, C^+ ion and proton H^+ are remarkably homogeneous: $x(\text{O}) = 3 \times 10^{-4}$, $x(\text{C}^+) = 1.4 \times 10^{-4}$ (all C is photoionized at $G_0 = 1$) and $x(\text{H}^+) = 5 \times 10^{-6}$ result from the balance between cosmic ray ionization and H^+ recombination.

Similarly, it is expected that the abundance of OH results from the balance between the recombination of H_3O^+ (with branching ratio 2/3 towards OH, the other 1/3 going to H_2O) and the photodissociation of OH, with rate $R_3 = 2.9 \times 10^{-10} G_0 e^{-1.7A_{\text{O}}} \text{ s}^{-1}$:

$$\frac{x(\text{OH})}{n_{\text{H}}} = \frac{2}{3} 2.0 \frac{x(\text{O})x(\text{H}^+)}{G_0} e^{-227\text{K}/T} \text{ cm}^{-3}. \quad (9)$$

The agreement between this prediction and the situation in the simulation (see Fig. 12, bottom-left panel) is not as good as for H_3O^+ because the destruction rate of OH is a slow process and its abundance is not at chemical equilibrium. Note that in equation (9) we took care to separate on the right-hand side the temperature contribution (from the threshold effect of the charge exchange reaction $\text{H}^+ + \text{O} \rightarrow \text{O}^+ + \text{H}$) and on the left-hand side the density contribution (from two-body formation reactions versus photoreactions). A shock can contribute through the surge of heat due to the dissipation, or through the compression that persists further away in the wake of the shock. A shearing sheet would contribute only through the temperature surge. In Fig. 12 (bottom-

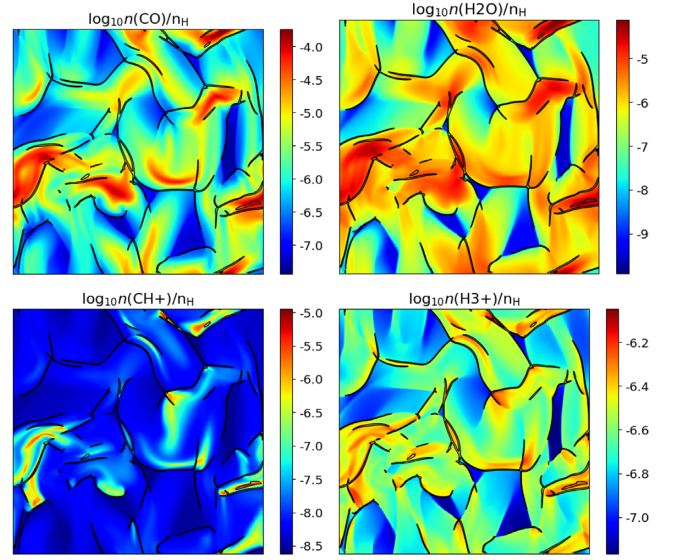


Figure 13. Relative abundance maps at $t = 300$ yr for a choice of species. Thin black contours of strong dissipation are overlaid.

left panel), the OH abundance above the dashed line is a footprint of a previous episode of stronger heating or compression.

CO results from ion-neutral reaction $\text{OH} + \text{C}^+$ (with rate $R_3 = 1.6 \times 10^{-9} \text{ cm}^3 \text{ s}^{-1}$) followed by hydrogenation to give HCO^+ , whose dissociative recombination yields CO. If we assume that these three reactions are fast, we can use equation (9) to compute the rate of reaction of OH with C^+ and balance it against the photodissociation rate of CO (about $G_0 \times 3.5 \times 10^{-11} \text{ s}^{-1}$ in the irradiation conditions of our simulation):

$$x(\text{CO}) = n_{\text{H}}^2 \frac{2}{3} \frac{x(\text{H}^+)x(\text{O})x(\text{C}^+)}{G_0^2} e^{-227\text{K}/T} 90 \text{ cm}^6. \quad (10)$$

Here, it can be seen that the effect of compression (n_{H}) is even more important than for OH. This is because higher density helps against photodissociation of both OH and CO. However, the match with the simulation is now much worse, although the scaling with n_{H}^2 is roughly visible; see Fig. 12 (bottom-right panel), where the white dashed line represents equation (10) without the exponential temperature dependence. Indeed, equation (10) assumes equilibrium, which is even harder to realize due to the long photodissociation time-scale of CO (900 yr; i.e. comparable to the large-scale turnover time).

Surprisingly, CH^+ is also among the molecules whose total abundance is significantly enhanced (by a factor of 10, although for about 100 yr of time only; see Fig. 5), despite our neglect of ambipolar drifts. We show in Section 3.4.5 how this is linked to the excitation of H_2 levels.

3.4.3 Abundance maps

Molecular production seems to be located in the wake of the strong dissipation regions (see Fig. 13). CO, OH (not shown, but similar to CO) and H_2O can be locally enhanced by three to almost five orders of magnitude. This is due both to the temperature threshold effect for the charge exchange reaction $\text{O} + \text{H}^+$ and to the compression effect, which protects molecules against photodissociation as discussed above, and so CO, OH and H_2O have similar maps. By contrast, H_3^+ is more mildly tied to the temperature, and so shows less marked variations. Finally, CH^+ is strongly enhanced only in the

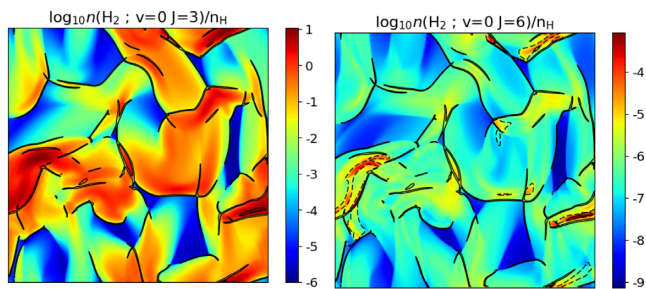


Figure 14. Map of the relative abundance (log scale) of the upper level of H₂ S(1) ($J = 3$, left panel) and the level $J = 6$ (right panel) at $t = 300$ yr. Thin black contours of strong dissipation are overlaid. The maxima of the level $J = 6$ often coincide with the peaks of CH⁺ abundance (marked on the right panel as grey dashed contours where $n(\text{CH}^+)/n_{\text{H}} = 10^{-6.5}$).

hottest regions, which suggests a sharp temperature threshold effect, although the temperature threshold for its formation reaction $\text{C}^+ + \text{H}_2 \rightarrow \text{CH}^+ + \text{H}_2$ is 4600 K, way above the maximum temperature of the simulation at that time (around 850 K). We show that this is linked with the H₂ excitation in Section 3.4.5.

3.4.4 H₂ excitation

Strong excitation of H₂ takes place in the wake of strong dissipation regions (see Fig. 14). In particular, the third rotational level of H₂ can be locally enhanced by nearly seven orders of magnitude compared with its value in the initial conditions: this should produce huge contrasts in the emissivity of the 0–0S(1) line of H₂. However, the ortho-to-para ratio is almost homogeneous (not shown): the conversion of ortho to para states is very slow compared with the thermalization of excited levels within even and odd states. The ortho-to-para thermalization occurs on much longer time-scales than the dynamical times in the simulation. The smaller range of variation of the higher-energy levels gives some a posteriori justification for the use of a maximum rotational number $J_{\text{max}} = 6$.

3.4.5 CH⁺ formation

Shortly after the surprising detection of large abundances of CH⁺ in the ISM (Douglas & Herzberg 1941), there were a number of tentative explanations to explain the boost of endoergic routes of formation for CH⁺. Elitzur & Watson (1978) proved that shock heating could overcome the temperature threshold of the $\text{C}^+ + \text{H}_2$ reaction to produce CH⁺, but their models produced copious amounts of OH as well, which was not observed. Draine & Katz (1986) and Pineau des Forêts et al. (1986) then showed how ion-neutral reactions could be enhanced by the ion-neutral drift due to ambipolar diffusion in C-type shocks, with the result of producing CH⁺ with temperatures below the activation barrier for OH formation. Falgarone et al. (1995) and Joulain et al. (1998) have shown how incompressible dissipation bursts can provide the necessary heat to generate molecules. Godard et al. (2009) and Godard, Falgarone & Pineau des Forêts (2014) later included the effect of the ion-neutral drift, which helps to enhance CH⁺ with respect to OH, as required by observations. Lesaffre et al. (2007) suggested that contact between the atomic warm neutral medium and the cold molecular interiors of diffuse clouds could help gather C⁺ and H₂ in an environment sufficiently warm to trigger the formation route of CH⁺ at the cloud interfaces. Valdivia et al. (2016) proposed that H₂ chemistry of fluid parcels adapts too

slowly to their multiphase condensation and evaporation history or to their alternating shielded and irradiated periods. This could explain the presence of warm H₂ susceptible to produce CH⁺ at the edge of clumps (see Valdivia et al. 2017). Agúndez et al. (2010) and Zanchet et al. (2013) suggested that H₂ excitation can help skirt the formation threshold, and thus play a role in CH⁺ formation. We show below in this subsection that this is the mechanism at play in the present work.

Dove & Mandy (1986) formulate a method to compute the state-to-state rates of endoergic reactions with excited H₂, using state-to-state thresholds lowered by the excitation energy of the H₂ level considered: they use this formalism for H₂ collisional dissociation. Lesaffre et al. (2013) implement this method in the Paris–Durham shock code for the $\text{C}^+ + \text{H}_2 \rightarrow \text{CH}^+ + \text{H}$ reaction. We use the same implementation here, which follows the prescription by Agúndez et al. (2010).

In the present simulation at age 300 yr, CH⁺ formation coincides exactly with places where the $J = 6$ level has a high abundance (see Fig. 14). This level has an energy of $E_6/k = 3470$ K, which closes a good fraction of the energy gap of 4300 K necessary to produce CH⁺: even a mild temperature of 800 K can alleviate the threshold from this level. On average, over the computational domain at $t = 300$ yr, 90 per cent of the formation rate of CH⁺ comes from the $J = 6$ level. The average rate of formation for the $\text{C}^+ + \text{H}_2 \rightarrow \text{CH}^+ + \text{H}$ reaction is increased by more than 200 times compared with what the Hierl, Morris & Viggano (1997) rate would give and by a factor of 1300 when compared with the Gerlich et al. (1987) rate. This raises the question of whether we should employ the same state-to-state rates for other endoergic reactions such as the $\text{O} + \text{H}_2 \rightarrow \text{OH} + \text{H}$ reaction, which is subject to a 3000 K temperature threshold and could well benefit similarly from H₂ excitation. It would then pave the way to enhance even more the production of other molecules such as H₂O or CO. This calls for the necessity of computing such state-to-state rates, with all the complexity this implies.

4 THE ROLE OF SHOCKS

The above exploration suggests that molecule production, excitation, compression and heating are tied to dissipation. In this section, we draw a more detailed link between dissipation, chemistry and the shock fronts in the simulation.

4.1 Shock front extraction procedure

We select three epochs where we carefully examine the dynamical fields and try to interpret them as a collection of shocks: epoch I ($t = 300$ yr), epoch II ($t = 1100$ yr) and epoch III ($t = 3000$ yr).

We first find the ridges of strong dissipation by applying DISPERSE (Sousbie 2011) to the dissipation field. This algorithm detects the spines of the ridges as a list of pixel vertices, which makes it cumbersome to define the local direction of the filament’s spine. Hence, we smooth each filament identified by DISPERSE using cubic B-splines with a smoothing condition of a width of 5 pixels (scipy.interpolate.splprep implementation of Dierckx 1982). The smoothed filaments are overlaid on the dissipation field in Fig. 15. Even though the algorithm does a good job even in crowded hubs, we note the detection is not completely exhaustive, as many endings are missed.

We then parse each filament along its length: every 10 pixels, we compute tangential and normal unit vectors to the filament. We inspect the dissipation field along the normal vector to find the pixel

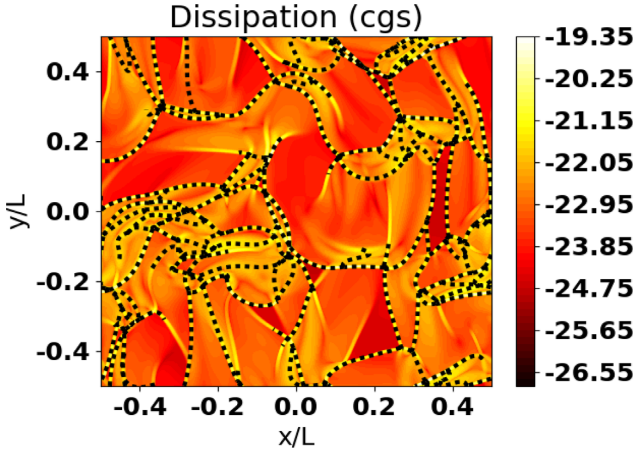


Figure 15. Smoothed DISPERSE dissipation filaments (dotted lines) overlaid on the dissipation field (log scale of the rate in $\text{erg cm}^{-3} \text{s}^{-1}$) at time $t = 300 \text{ yr}$.

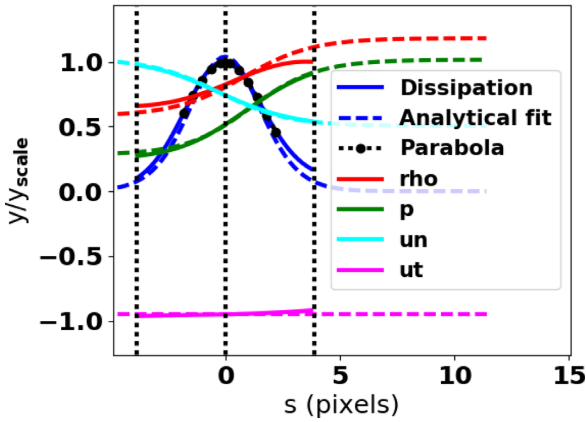


Figure 16. A typical ($r^2 = 0.0058$) shock adjustment at epoch I. The five quantities $\ln \epsilon$ (log of dissipation, blue), ρ (mass density, red), p (pressure, green), u_n (normal velocity, cyan) and u_t (tangential velocity, magenta) that take part in the fit are displayed, normalized by their relevant scales so that their contribution to the residuals is directly visible. Solid lines are the profiles interpolated in the simulation, dashed lines are the best-fitting analytical model from Appendix A2. Vertical dotted lines indicate the region of the fit and the position of the shock ($s = -\ell, 0, +\ell$), labelled in pixels. The black dots illustrate the parabolic adjustment of the log of dissipation, which we use to find the origin of the profile and the curvature radius ℓ . The adjusted shock model has speed 1.34 km s^{-1} (Mach number 1.76) and entrance density $n_{\text{H}} = 65 \text{ cm}^{-3}$.

where the maximum of the dissipation lies and we set this point as the origin of distances along the normal (see Fig. 16). We find in which direction the density field grows, and we set this direction as a positive coordinate along the normal. We now interpolate all fields along this direction with a sampling rate of a fifth of a pixel to build a 1D profile of every relevant dynamical variable: mass density ρ , perpendicular (along the normal) u_n and transverse (along the tangent) u_t velocities, pressure p , and dissipation field ϵ . We fit a parabola to the logarithm of the dissipation field to fine tune the position of the maximum dissipation, which we set as the new origin of coordinates along the profile. We use this parabola to compute the curvature radius at maximum dissipation as $\ell^{-2} = -(\partial^2 \ln \epsilon / \partial s^2)|_{\epsilon=\epsilon_{\text{max}}}$ (where s is the coordinate along the normal to the filament; see the vertical dotted lines in Fig. 16). We discard

this position if it lies closer than ℓ to an edge of the domain, to avoid issues with its periodicity.

We make a first guess for the shock entrance velocity u_0 in its steady-state frame, by using

$$u_0 = \frac{\rho(\ell)u_n(\ell) - \rho(-\ell)u_n(-\ell)}{\rho(\ell) - \rho(-\ell)}, \quad (11)$$

which comes from the requirement of mass conservation in the steady-state shock frame; note that Rankine–Hugoniot requires $\rho(u - u_0)$ to be constant. We use this first-guess velocity to transform the velocity u_n to a shock frame velocity and to estimate steady-state frame mass, momentum and energy fluxes \dot{M} , \dot{Q} and \dot{E} (Appendix A2) along with the constant transverse velocity u_{t0} . We finally adjust the five parameters u_0 , u_{t0} , \dot{M} , \dot{Q} and \dot{E} in the analytical solution of Appendix A2 starting from these first-guess estimates until the minimum of the sum of the normalized profile averaged square residuals of ρ , u_n , u_t , p and ϵ is reached. In other words, we minimize the dimensionless residual,

$$r^2 = \sum_{y \in \{\rho, u_n, u_t, p, \epsilon\}} \left\langle \left(\frac{y - y_{\text{analytics}}}{y_{\text{ref}}} \right)^2 \right\rangle_{\text{profile}}, \quad (12)$$

which should be small when the analytical model is a good representation of the simulation profile. The reference values to normalize these quantities are defined as their maximum values within a distance ℓ to the maximum dissipation position (the domain where we restrict the shock profile adjustment). Note that we do not fit for the viscous coefficient, as we keep it fixed to the input value used in the hydrodynamic computation; we have shown that the resolution is high enough so that the extra viscosity due to the numerical scheme is negligible. Because the resulting residuals r^2 we achieve are typically well below 1 (median 6×10^{-3} , best value 3×10^{-4} for epoch I on the selected shocks), we are confident that this is indeed the case. A typical example is illustrated in Fig. 16.

When the residual r^2 is below 0.1, and the shock entrance velocity is above the speed of sound, we identify this point as a shock and record its parameters. Fig. 17 displays all shocks fulfilling these conditions as black arrows proportional to the shock entrance velocity overlaid on the dissipation field.

We used the method SHOCK_FIND as described in Lehmann, Federrath & Wardle (2016) to extract shock parameters and compare them with our current method. For each shock position found in our simulation, we use the local direction of the shock (as opposed to the density gradient proposed by the SHOCK_FIND method) and we define the pre-shock density and shock velocity as in steps (iv) and (v) of Lehmann et al. (2016). We use $N_{\text{pix}} = 6$, which means pre- and post-shock values are taken 3 pixels before and after the maximum of dissipation. We compare the resulting entrance velocity and density for our shocks in Fig. 18. The agreement for the entrance density is good, with a small scatter. However, there is a larger scatter for the velocity, and there seems to be a small bias between both our methods, with SHOCK_FIND finding larger values at larger velocities, and smaller values at lower velocities. In particular, SHOCK_FIND finds Mach numbers slightly below 1 for most of the lowest velocity shocks (for which our method finds values slightly above 1), and would not have labelled them as shocks. One dissipative structure is even detected by SHOCK_FIND as a negative velocity shock, and inspection of the profile at this position shows that there is virtually no velocity jump, which puts the result of our fit into question in this isolated case. The discrepancy at larger velocity may introduce some bias in the statistical distribution of

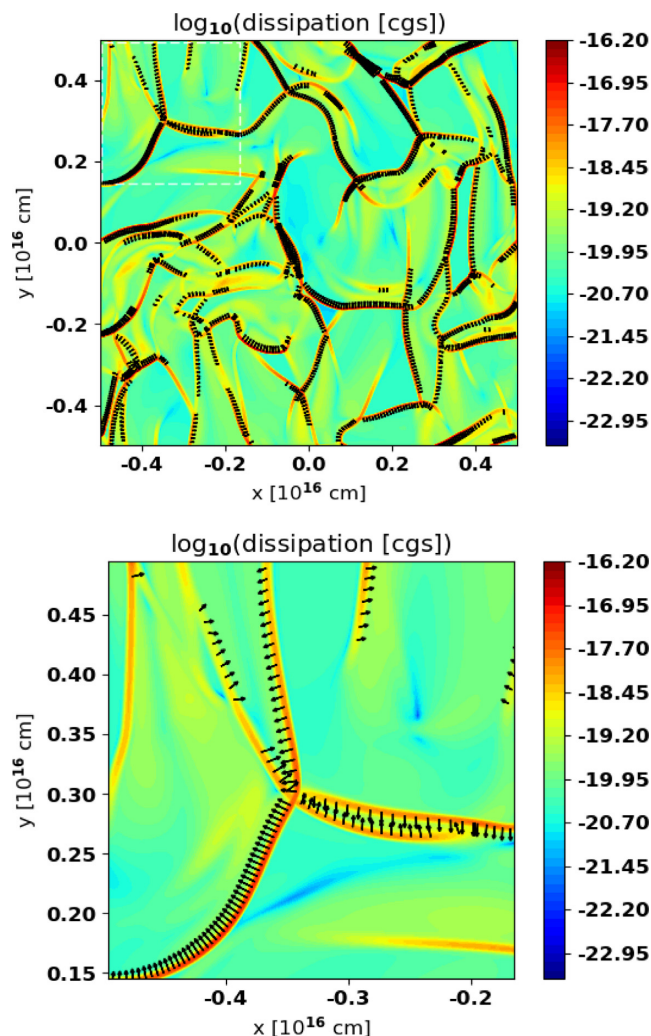


Figure 17. Detected shocks (black arrows, proportional to the entrance velocity, pointing towards the post-shock region) overlaid on the dissipation field (log scale) at epoch I, $t = 300$ yr. The bottom panel is an enlargement of the top left of the top panel (in the region delineated by white dashes). Note that shocks are associated with compressible dissipation (see Fig. 8).

velocities, with our method yielding lower probabilities for large velocities than SHOCK_FIND would.

4.2 Shock statistics

Fig. 19 illustrates the statistics of the entrance velocities and densities experienced in our detected shocks for the three epochs in the simulation. The number of shocks detected (see Table 2) decreases as time proceeds and kinetic energy decays towards a more quiescent flow (so does the average entrance velocity). The dispersion around the mean values for velocities and densities also decreases as turbulence damps away (see Table 2). Note that velocities are biased towards large velocities at early times, but we do not have enough statistics to characterize the shape of the distribution. Because of the total mass conservation, local compression of matter has to be compensated by large volumes of lower density, and shock fronts are more likely to run into dilute material. As the average entrance velocity decreases in time, the average entrance density increases. Also, the bias of entrance

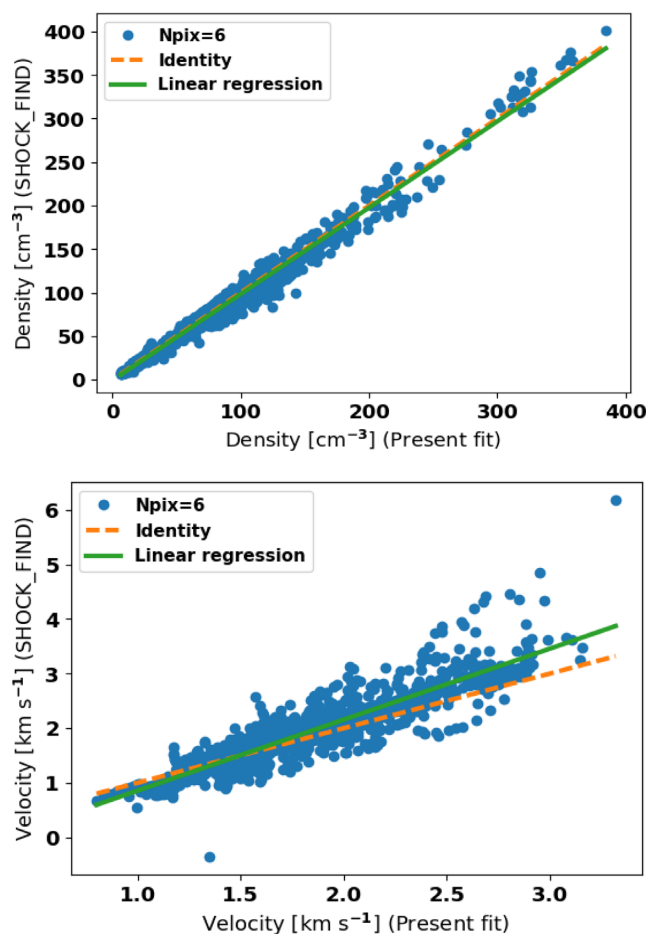


Figure 18. Comparison between SHOCK_FIND (y-axis) and our method (x-axis) for the pre-shock parameters: density (top) and velocity (bottom). Linear fits (solid lines) are overlaid, which can be compared with the identity line (dashed line).

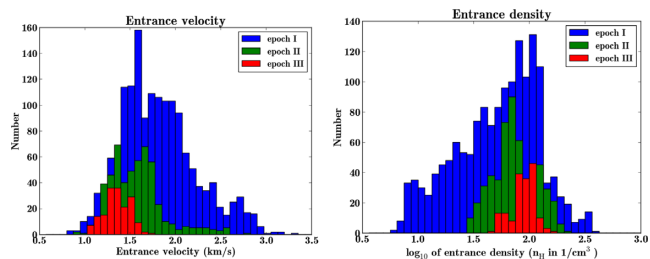


Figure 19. Histogram of the entrance velocities (left panel) and densities (right panel) in the detected shocks at three epochs: blue for epoch I ($t = 300$ yr), green for epoch II ($t = 1100$ yr) and red for epoch III ($t = 3000$ yr).

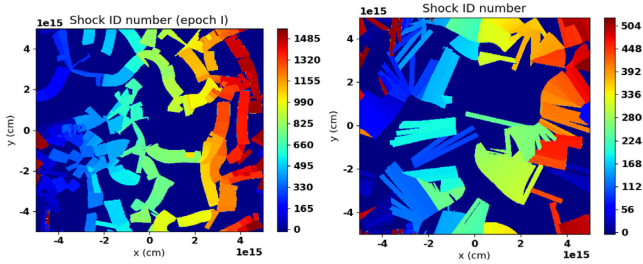
densities towards lower values results from the bias of velocities towards large values.

4.3 Shock wakes

For each detected shock at each epoch, we measure its entrance parameters in the simulation: temperature, composition and ortho-to-para ratio. We then run a 1D steady-state model with the Paris–Durham shock code. As our simulations include no magnetic field, all these models are J-type shock models. Their steady-state time

Table 2. Fraction of various dissipative heatings over various regions of the simulations. Fronts are defined as being less than 10 pixels away from detected shocks. Wakes are defined as the influence regions of shocks (see Section 4.3 and Fig. 20).

	Epoch I (300 yr)	Epoch II (1100 yr)	Epoch III (3000 yr)
Number of shocks	1552	522	170
Average shock entrance velocity in km s^{-1} (\pm standard deviation)	1.82 ± 0.42	1.56 ± 0.29	1.36 ± 0.14
Average shock entrance density in cm^{-3} (\pm standard deviation)	71 ± 57	81 ± 37	90 ± 21
Volume fraction of shock wakes	57%	72%	32%
Mass fraction in shock wakes	72%	80%	37%
Viscous compressive heating total fraction ($(\epsilon_{\text{comp}})/(\epsilon_{\text{viscous}})$)	77%	64%	42%
Fraction of dissipation in shock fronts ($(\epsilon_{\text{viscous}})_{\text{fronts}}/(\epsilon_{\text{viscous}})$)	67%	54%	27%
Fraction of dissipation in shock wakes ($(\epsilon_{\text{viscous}})_{\text{wakes}}/(\epsilon_{\text{viscous}})$)	74%	85%	51%
Vortical heating fraction in shock wakes ($(\epsilon_{\text{vort}})_{\text{wakes}}/(\epsilon_{\text{vort}})$)	81%	85%	44%
Compressive heating fraction in shock wakes ($(\epsilon_{\text{comp}})_{\text{wakes}}/(\epsilon_{\text{comp}})$)	79%	87%	61%

**Figure 20.** Map of the shock number of every pixel at epoch I ($t = 300$ yr, left) and epoch II ($t = 1100$ yr, right). Background pixels that do not fall in any shock influence zone are given the value -1 (darkest blue colour).

(defined as the time it takes for the thermal state of the gas to return to equilibrium) is of the order of 1000 yr. We truncate the model at a time corresponding to the epoch considered, which allows us to mimic snapshots at various stages in the shock evolution (see Lesaffre et al. 2004b). We use the total length of the steady-state model as an estimate for the maximum extent of the shock perpendicular to the shock front in the 2D simulation. We define the lateral extent of the influence zone of each shock as 20 pixels (slightly larger than the 10 pixel separation between shocks on their dissipation filament, as this allows for potential convexity of the shock front). When a pixel falls in the influence zone of several shocks, we connect it to the closest shock and we record its orthogonal distance to the shock front, so we can later match it to a given position in the 1D steady-state model. Some pixels are outside any shock influence zone, and we define these as ‘background’ pixels. Other pixels are ‘shock wake’ pixels and they all have one shock connected to them: the map of the shock number of each pixel at epochs I and II can be seen in Fig. 20. The shock wakes at late times are thicker than at early times due to the larger age of the shocks, which increases the extent swept by each shock. We also define a ‘shock front’ region, which encompasses all pixels within a distance of 10 pixels from a detected shock position: this region follows closely the ridges of strong dissipation, while the shock wakes trail behind. In other words, shock wakes trace the fluid that has been influenced by shocks, while shock fronts trace the fluid that is currently being processed.

4.4 Dissipation in shocks

We evaluate here how much of the dissipation this collection of shocks can explain. We first compute the dissipation heating budget from shocks at the three epochs we have considered. The results

are summarized in Table 2: adiabatic shock fronts (without their relaxation wake) amount to about two-thirds of the total dissipation at the maximum of dissipation (near epoch I), but this fraction decays to only a quarter at later times. Most of the compressive heating can be accounted for by shock front heating. The remainder is probably in weaker compressive waves (such as dying shocks or the weaker lateral sides of shocks) and in missed shocks (close to edges of the simulation, for example, or near the endings of dissipation ridges). Furthermore, as suggested by the green colour trailing the blue ridges in Fig. 8, most of the vortical heating is localized in the wake of shocks. Overall, nearly 80 per cent of the total dissipation takes place in shock wakes at epochs I and II. At epoch III, most shocks have disappeared, but their wakes are longer, so they still account for half of the total dissipation.

4.5 Molecular yields and excitation in shocks

We now attempt to model the 2D simulation results by using a collection of 1D steady-state shock models.

Now that each shock wake pixel is associated with a position in a steady-state shock, we can model any variable by its value as given by the outcome of the Paris–Durham shock code. We detail the comparison for one shock example in Fig. 21. There are considerable differences between the 1D steady-state models (nearing a factor of 10 for chemical abundances in the worst cases) and the time-dependent 2D simulation, but the overall behaviour of the fluid physical and chemical state variables is recovered and the relative differences are usually significantly less than the global span of the variables.

We complement the 1D models in the shock wakes by connecting background pixels with the relative abundances corresponding to thermal and chemical equilibrium at the local density in the simulation. We compare the resulting modelled CO maps to the actual snapshots of the time-dependent simulation shown in Fig. 22.

At epoch I, the differences between modelled abundances and actual abundances in the shocked regions can be large, but these differences are generally significantly smaller than the overall span of the CO composition (one order of magnitude versus three orders of magnitude; compare the width of the blue histograms in the rightmost panels of Fig. 22 to the full span of the colour bar of the middle panels). Also, the differences have a symmetric distribution around zero, which suggests they might average to a small number. However, the situation in the background regions is much worse, with background steady-state abundance systematically underestimating the actual CO composition (see orange histograms in the

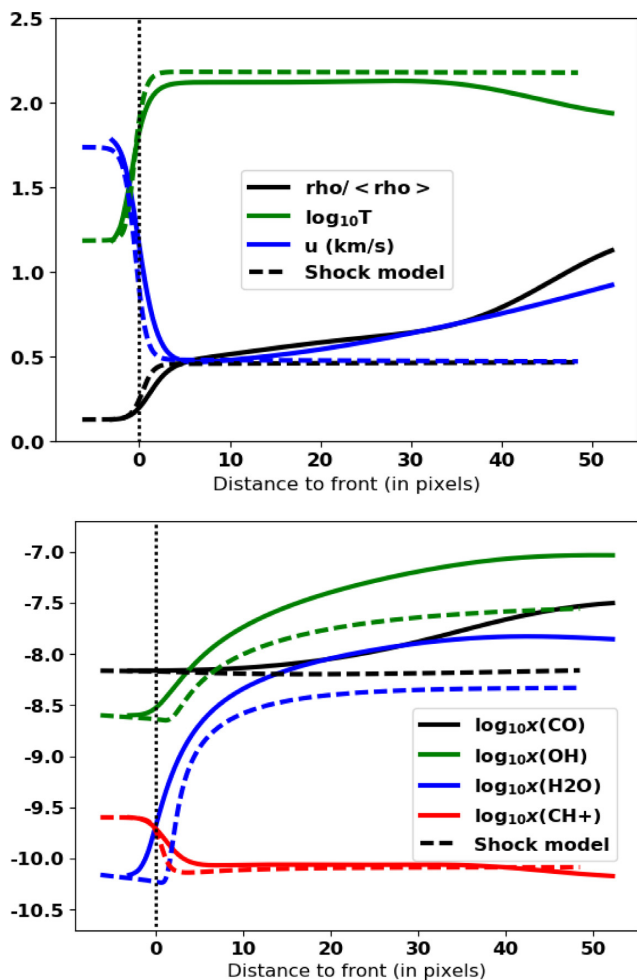


Figure 21. Comparison between Paris–Durham steady-state shock (dashed) and time-dependent simulation (solid lines) for one of the shocks detected at epoch I: hydrodynamical variables in the top panel, and chemical abundances in the bottom panel. Initial conditions are the same, and they are read on the simulation pre-shock position. The shock front position is marked for reference as a vertical dotted line.

rightmost panels of Fig. 22). In some places, near the centre of the figure at position $(0, 0.15 L)$, a finger of CO is completely missed out by the steady-state modelling. This can be traced back to the shock detection method. A close inspection of the pressure field movie (see Fig. 11) shows that, at this position, a shock catches up with another shock. Its front runs into hotter fluid, and its entrance Mach number falls below 1. This shock now becomes a weak compression wave and it is about to die out, but its chemical yields are still present, trailing behind what used to be a shock.

At epoch II, the large extent of the shock influence region due to the larger time-scale shows the limitations introduced by our arbitrary sideways extension of the influence zone (and it is even worse for epoch III). The background region is now filled out with out-of-equilibrium gas, and the steady-state chemical equilibrium completely fails to reproduce the abundances. Shock wakes fare better, with still positive and negative differences, and relative differences are not worse than at epoch I. Bear in mind that the collection of 1D model runs in about two CPU hours, whereas the actual 2D simulation takes about 50 000 times more.

The differences can be attributed to many factors that have been neglected in the steady-state modelling: curvature effects,

vortical dissipation in the shock wake, obliqueness of the shock trajectory behind the fronts, sideways gradients or diffusion (thermal or chemical) between adjacent shocks, transverse compression or dilatation, pre-shock H_2 levels not following Boltzmann equilibrium in the 2D simulation while they do in 1D, intrinsic non-steadiness of the shock front and its relaxation layer, and sensitivity of the shock radial extent to the shock front history.

Despite these potential drawbacks, the resulting maps provided by the steady-state modelling are globally quite satisfactory. The statistical distributions of the differences between the models and the actual simulation for CO (rightmost panels of Fig. 22) suggest looking at the average numbers for CO and other molecules.

We now examine integrated molecular contents at epoch I with the help of histograms in Fig. 23. For each species, we display coloured bars proportional to four integrated quantities. The blue and red bars represent the molecular contents in the simulation for the background and shock wake regions, respectively. The cyan and orange bars represent the molecular contents in the models for the background (chemical equilibrium) and shock wake (1D steady-state shocks) regions, respectively. All four bars are normalized to the total molecular content of the simulation at epoch I. Hence, the sum of the simulated shocked (red bars) and background (blue bars) fractions always amount to 1.

Shocked versus background fractions for simulations (red versus blue bars) or models (orange versus cyan bars) in Fig. 23 illustrate what fraction of the molecular production (or H_2 excitation) is realized in regions defined as shocked (red and orange bars) or background (blue and cyan bars). The H_2 molecule is present everywhere, and its background-to-shocked (blue/red or cyan/orange) fraction only reflects the roughly equal sharing between the volume of the shocked and background regions. The volume fraction of shocks is 57 per cent at epoch I and 72 per cent at epoch II (see Table 2). The corresponding mass fraction is about 10 per cent larger than the volume fraction: compression in shocks gives a slight edge to the mass of shocked regions.

Shocked fractions (red and orange bars) are always of about the same size: when averaged over the shock wakes, the steady-state method gives answers very close (within 10 per cent for epoch I and 20 per cent for epoch II) to the actual simulation. This is a key result of the present study. The steady-state model performs best when the pre-shock chemical composition and the temperature are extracted from the time-dependent simulation. We have checked that the initial chemical equilibrium is not critical for the model. However, we have found that the pre-shock temperature can have a significant role. Indeed, for low-velocity shocks, the thermal energy can be a significant fraction of the ram pressure in the pre-shock. It can then control, in part, the post-shock pressure, and hence the amount of compression in the post-shock, and so the molecular yields for those species that sensitive to compression. We have also checked that the pre-shock ortho-to-para ratio is critical in determining the saw-tooth patterns of the post-shock H_2 excitation diagram (as shown in shock models by Wilgenbus et al. 2000; Neufeld & Yuan 2008). Although in the present case this ratio is almost uniform due to the small size of the computational domain, a statistical distribution of ortho-to-para ratios may be necessary to accurately represent a large spatial extent of gas in the ISM.

The comparison between shock models (orange bars) and chemical equilibrium (cyan bars) shows that some molecules and excited H_2 levels are very sensitive to shock chemistry (orange dominates over cyan). This shows the effect of the compression, heating and

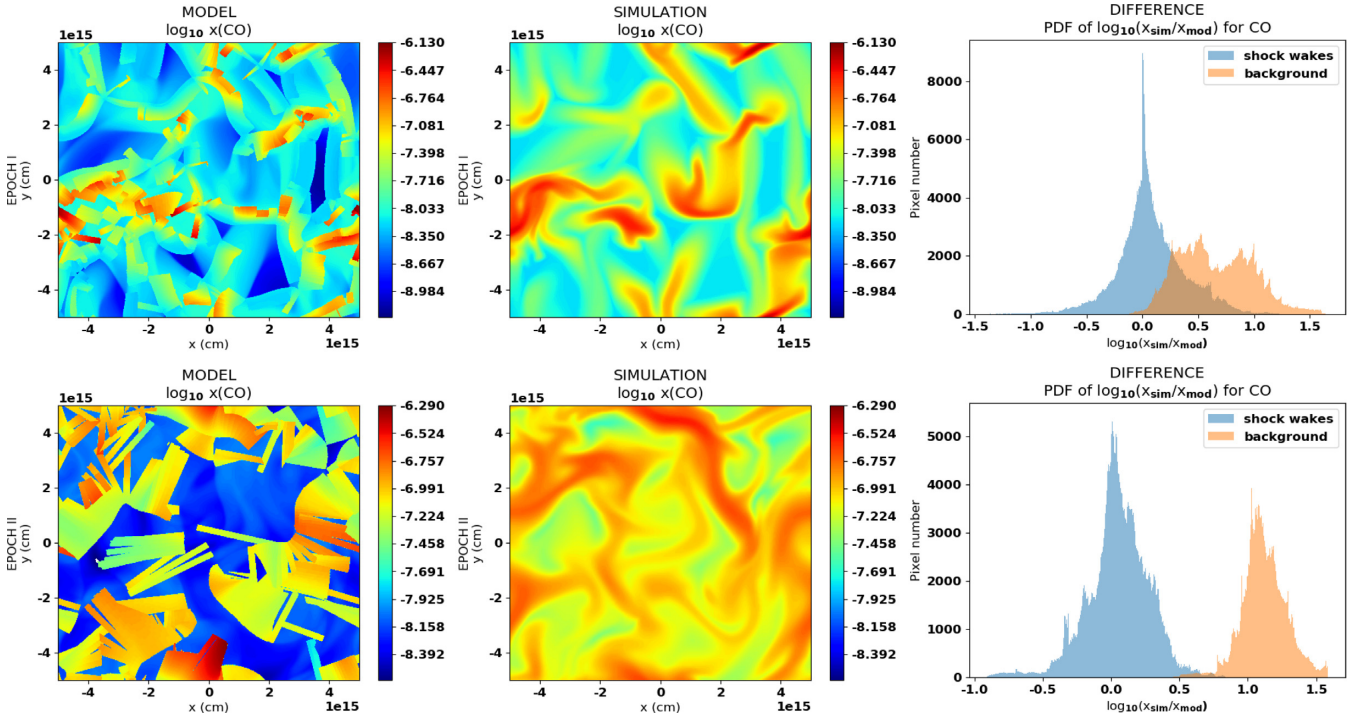


Figure 22. Steady-state shock modelled by Paris–Durham (left) and actual simulation outcome from CHEMSES (centre) for maps of CO at epoch I (top) and at epoch II (bottom). Colour scales for modelled and actual maps have been matched for easier comparison. Probability distribution functions of relative differences between the simulation and models in shock wakes and background region are also shown (right).

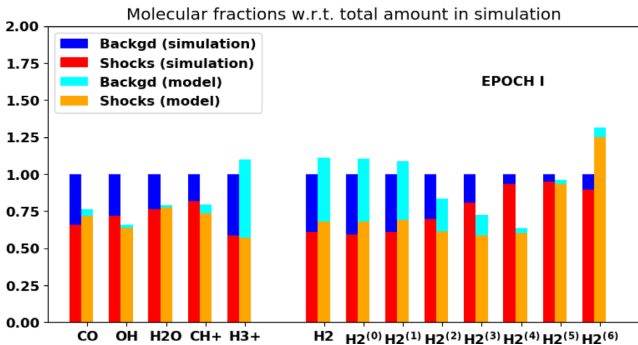


Figure 23. Computational domain averaged molecular yields and H_2 excitation at epoch I, normalized by the results of the 2D simulation. Red and blue histograms show the fraction of molecules present in the shock wake (red) and background (blue) regions. Cyan and orange histograms show the total amount of molecules in shock wake (orange) and background (cyan) regions in the maps modelled by the steady-state shocks, normalized by the answers given by the actual 2D simulation. The right-hand side of the plot shows similar histograms for various H_2 levels with superscripts labelling their rotational quantum numbers (J).

excitation, which for the latter two helps overcome temperature thresholds.

This is less striking for the shocked versus background fractions of molecules in the simulation (red versus blue bars). This is presumably because of our lack of precision when we circumscribe the shocked regions: as discussed above, the background region sometimes contains former shocks. These missed shocks probably account for the large discrepancies between the steady-state model and the simulation in the background region (blue versus cyan bars). In other words, large ratios of simulated versus modelled

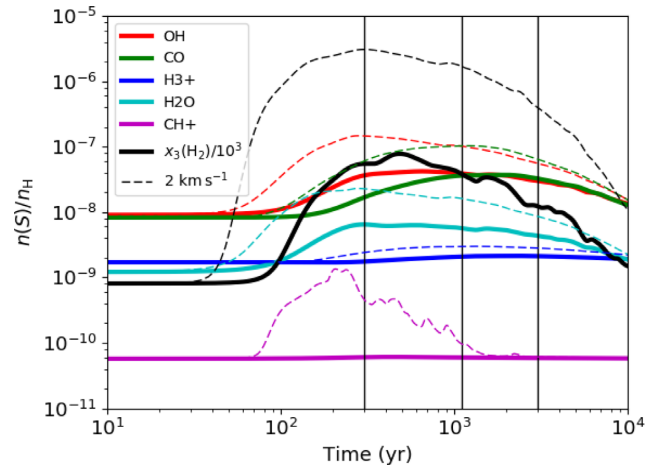


Figure 24. Time evolution of the average composition as in Fig. 5, but for initial conditions with $\sqrt{\langle u^2 \rangle} = 1 \text{ km s}^{-1}$. Dashed lines recall the results for $\sqrt{\langle u^2 \rangle} = 2 \text{ km s}^{-1}$ displayed in Fig. 5. Vertical black lines mark the three epochs we considered.

background (blue versus cyan bars) identify species sensitive to dissipative chemistry.

The initial rms velocity is likely to have a strong impact, as it will determine the temperature and thus which thresholds are likely to be overcome or not. Fig. 24 illustrates this on the average evolution of the composition for an initial rms velocity of 1 km s^{-1} instead of 2 km s^{-1} . The molecular yields are significantly weaker, and the H_2 excitation is much lower. As a result, there is no production enhancement for CH^+ .

Our initial 2D Fourier spectrum is a top-hat for $k \leq 5k_0$. This means that the total power is largest in the annulus at $k = 5k_0$,

so the initial velocity field has slightly more power at a fifth of the box size. This probably sets the average distance between shocks, and it might be a critical parameter for how often a fluid parcel experiences shock processing, which may control the chemistry of slowly reacting species. Hence, future studies will also have to investigate the influence of the initial velocity perturbation.

5 CONCLUSIONS AND PROSPECTS

We consider, for the first time, the interplay between dissipation, chemistry and molecular hydrogen excitation in multidimensional hydrodynamics. In order to resolve the dissipation scales, the computational domain has been reduced to an extremely small size. The initial conditions for the rms velocity are quite large compared with observed quantities for this size, but its average over the whole duration of the simulation falls within observational bounds (see fig. 6 in Falgarone et al. 2009). The whole computational domain should be considered as a small fluid parcel, which passes through a larger-scale dissipative structure: it experiences a burst of velocity dispersion at the beginning of the simulation, which quickly decays. The present detailed simulations constitute a unique proof of concept to carefully examine both the chemistry (and molecular excitation) and the dissipation at the same time.

In this 2D experiment, dissipation lies on well-defined ridges (see Fig. 8), which we characterized using the DISPERSE algorithm (Sousbie 2011; Sousbie, Pichon & Kawahara 2011). Because of an analytical solution, we identified shock fronts along these ridges. We affected every pixel in their wake to a 1D steady-state shock model and were thus able to recover maps of the simulation using corresponding truncated steady-state shock models. We examined the statistics of these parameters, which show a much higher number of shocks in the lower half range of velocities and which exhibit a tail at large velocities. The dissipation in all shock fronts accounts for nearly 80 per cent of the dissipation in the computational box at its highest peak. This remains valid for a significant amount of time if one includes the shock wakes. Shocks are very efficient at producing molecules, mainly as a result of the dissipation heating that helps trigger chemical routes, and the increase in particle density due to compression behind the shocks, which helps molecules survive photodissociation. The average composition in steady-state shocks matches very closely the actual simulation results over the shocked region (to within ± 20 per cent for most species of interest). Despite the huge number of approximations (steadiness and neglect of front curvature, of sideways gradients along the front, of dilution effects, etc.), local errors cancel when globally averaged.

One straightforward improvement would be to investigate the effect of ambipolar diffusion in the same set-up. By introducing ion-neutral drift velocities, ambipolar diffusion considerably enhances the chemical rates of ion-neutral reactions, giving birth to a specific chemistry controlled by magnetic fields, whose signatures in the diffuse ISM match observations, as demonstrated by Godard et al. (2009, 2014). Ion-neutral reactions, such as the one leading to the formation of the CH^+ molecule, are potentially strongly enhanced by ambipolar diffusion, provided drift velocities can reach large values, which remains to be ascertained (Valdivia et al. 2017). The steady-state shocks models would then have to account for magnetized J-type, CJ-type, C*-type and C-type shocks (Godard et al. 2019) and their intermediate time-dependent CJ-type counterparts (see Lesaffre et al. 2004b). The ion-neutral drift might then drown the H_2 excitation effect we found for CH^+ in this study.

Although the present simulation considers only a very small domain (the whole extent of the present simulation corresponds to barely one pixel of the best-resolved 3D simulations of the ISM), it demonstrates that small-scale chemical production and excitation can be important. Such chemical yields are in fact absent from large-scale simulations of the ISM, even when they compute the hydrodynamical and chemical evolutions simultaneously. In the simulations by Glover et al. (2010), for example, the resolution is too sparse to resolve not only the dissipative scales (10^{14} cm), but even the cooling scales (10^{16} cm). Nearly every modern computational fluid dynamics algorithm preserves energy, so the energy dissipated in a shock with given entrance conditions (such as entrance speed, for instance) is the same regardless of the resolution. However, in large-scale simulations, the dissipation rate is smeared out over a few computational zones, which is usually considerably larger than the actual physical dissipation scale in the interstellar medium. Resulting shocks at low resolution are hence nearly isothermal, and warm chemistry cannot be triggered in their fronts: molecules such as CO, which once formed can survive a long time in the wake of the shock front, are missed out. As the dissipative scales are way out of reach of current computational capabilities, we need subgrid models for the chemistry linked to dissipation.

Despite the local discrepancies between 1D steady-state models and local cuts of the 2D time-dependent simulation (see Fig. 21), the global average of molecular yields is satisfactory. This gives some justification for using statistical collection of shocks to interpret data (see Lesaffre et al. 2013, for example), and opens the way to subgrid models. Indeed, once we understand the statistics of shocks in 3D turbulence on the one hand, and the detailed chemistry and micro-physics of 1D shocks on the other hand, we can use a steady-state modelling approach to deduce detailed observational properties of the tracers of turbulence in various environments. We can paint the dissipative statistics with detailed thermal and chemical models and it will hopefully help us design new subgrid models, to better take into account the effects of turbulence dissipation in large-scale 3D simulations.

However, one must bear in mind that the statistics of rare events are hard to measure, and unfortunately the molecular yields and emissivities naturally give much more weight to the strongest dissipative events (i.e. the rarest). The task at hand is reminiscent of computing nuclear rates involving a Gamow-peak² effect as identified in the reconstruction of 3D bow-shock chemistry with 1D steady-state models (see Tram et al. 2018).

Conversely, multidimensional small-scale simulations will also help us improve 1D shock models in many other aspects. It will help us understand the way the post-shock pressure returns to the average pre-shock, how the shock is diluted back into the surrounding medium and dies out, and what instabilities are prone to distort the shock fronts. It will also help us to better understand the rate at which a given piece of fluid experiences successive shocks, thus giving insight into the typical entrance conditions in these shocks (and the variance around this typical value). Finally, once we master all aspects of the multidimensional dynamics, the 3D geometry of the shocks can be translated to 1D distribution functions, allowing us to build 3D models from 1D models in the same manner as for 3D bow shocks (Gustafsson et al. 2010; Tram et al. 2018).

²The product of the fast decreasing Maxwell–Boltzmann distribution with the steep turning on of tunnelling probabilities yields a sharp peak.

The effect of dissipation is particularly critical for the excitation of H₂ levels. Such models, which include the impact of dynamics on the molecular excitation, will hence be essential to prepare the future space missions such as *JWST* or *SPICA*, which are about to bring a wealth of high spatial resolution data on the H₂ emission lines obtained at unprecedented sensitivities. *SPICA*, in particular, with its fast survey capabilities, will act as an instrument of choice to investigate the large statistics required to assess the characteristics of turbulent dissipation. As for current instruments, the Very Large Telescope (Santangelo et al. 2014) and *SOFIA/EXES* are already providing detailed information on the H₂ line profiles (Neufeld et al. 2019; Reach et al. 2019). We plan to investigate the line shapes in our simulations in the near future.

Finally, we have demonstrated that the excitation of H₂ molecules can be critical to facilitate some chemical routes when they are blocked by temperature thresholds. Low-energy levels of H₂ can provide an intermediate step to bridge energetical gaps. This is especially striking for the formation of the CH⁺ cation in the present study, but we suspect similar phenomena might be at play, which could open formation routes for OH, en route to CO, and for the formation of SH⁺, a molecule with similar properties as CH⁺. This calls for a more careful investigation of the state-to-state chemistry of endoergic reactions and reactions with activation barriers, even though these effects might be dwarfed by ion-neutral drifts in the presence of magnetic fields.

ACKNOWLEDGEMENTS

We thank the anonymous referee for his thorough and detailed comments, which considerably improved the presentation of these results. Many thanks to S. Fromang for providing us with his version of DUMSES, from which CHEMSES was developed. The simulations were run on the jade machine at IDRIS under the project number c2012046804. This work was partly supported by the Programme National ‘Physique et Chimie du Milieu Interstellaire’ (PCMI) of CNRS/INSU with INC/INP co-funded by CEA and CNES. VV acknowledges support from the European Research Council (ERC) under the European Union’s Horizon 2020 research and innovation programme (MagneticYSOS project, Grant Agreement No 679937). The research leading to these results has received funding from the European Research Council, under the European Community’s Seventh Framework Programme, through the Advanced Grant MIST (FP7/2017-2022, No 742719).

REFERENCES

Agúndez M., Goicoechea J. R., Cernicharo J., Faure A., Roueff E., 2010, *ApJ*, 713, 662
 Black J. H., van Dishoeck E. F., 1987, *ApJ*, 322, 412
 Brown P., Byrne G., Hindmarsh A., 1989, *SIAM J. Sci. Stat. Comput.*, 10, 1038
 Dierckx P., 1982, *Computer Graphics and Image Processing*, 20, 171
 Douglas A. E., Herzberg G., 1941, *ApJ*, 94, 381
 Dove J. E., Mandy M. E., 1986, *ApJ*, 311, L93
 Draine B. T., 1978, *ApJS*, 36, 595
 Draine B. T., Katz N., 1986, *ApJ*, 310, 392
 Elitzur M., Watson W. D., 1978, *ApJ*, 222, L141
 Falgarone E., Pineau des Forets G., Roueff E., 1995, *A&A*, 300, 870
 Falgarone E., Verstraete L., Pineau des Forêts G., Hily-Blant P., 2005, *A&A*, 433, 997
 Falgarone E., Hily-Blant P., Pety J., 2009, in Lis D. C., Vaillancourt J. E., Goldsmith P. F., Bell T. A., Scoville N. Z., Zmuidzinas J., eds,

ASP Conf. Ser. Vol. 417, Submillimeter Astrophysics and Technology: A Symposium Honoring Thomas G. Phillips. Astron. Soc. Pac., San Francisco, CA, p. 243
 Federrath C., 2013, *MNRAS*, 436, 1245
 Flower D. R., Pineau des Forets G., 1998, *MNRAS*, 297, 1182
 Flower D. R., Pineau des Forêts G., 2015, *A&A*, 578, A63
 Flower D. R., Pineau des Forêts G., Hartquist T. W., 1985, *MNRAS*, 216, 775
 Flower D. R., Le Boulrot J., Pineau des Forêts G., Cabrit S., 2003, *MNRAS*, 341, 70
 Fromang S., Hennebelle P., Teyssier R., 2006, *A&A*, 457, 371
 Gerlich D., Disch R., Scherbarth S., 1987, *J. Chem. Phys.*, 87, 350
 Glover S. C. O., Federrath C., Mac Low M.-M., Klessen R. S., 2010, *MNRAS*, 404, 2
 Godard B., Falgarone E., Pineau Des Forêts G., 2009, *A&A*, 495, 847
 Godard B. et al., 2012, *A&A*, 540, A87
 Godard B., Falgarone E., Pineau des Forêts G., 2014, *A&A*, 570, A27
 Godard B., Pineau des Forêts G., Lesaffre P., Lehmann A., Gusdorf A., Falgarone E., 2019, *A&A*, 622, A100
 Grassi T., Bovino S., Schleicher D. R. G., Prieto J., Seifried D., Simoncini E., Gianturco F. A., 2014, *MNRAS*, 439, 2386
 Grete P., O’Shea B. W., Beckwith K., Schmidt W., Christlieb A., 2017, *Physics of Plasmas*, 24, 092311
 Gry C., Boulanger F., Nehmé C., Pineau des Forêts G., Habart E., Falgarone E., 2002, *A&A*, 391, 675
 Gustafsson M., Ravkilde T., Kristensen L. E., Cabrit S., Field D., Pineau Des Forêts G., 2010, *A&A*, 513, A5
 Hierl P. M., Morris R. A., Viggiano A. A., 1997, *J. Chem. Phys.*, 106, 10145
 Indriolo N., Fields B. D., McCall B. J., 2015, in American Institute of Physics Conference Series. p. 370
 Ingalls J. G., Bania T. M., Boulanger F., Draine B. T., Falgarone E., Hily-Blant P., 2011, *ApJ*, 743, 174
 Joulain K., Falgarone E., Pineau des Forets G., Flower D., 1998, *A&A*, 340, 241
 Kolmogorov A. N., 1962, *Journal of Fluid Mechanics*, 13, 82
 Lehmann A., Federrath C., Wardle M., 2016, *MNRAS*, 463, 1026
 Lesaffre P., Balbus S. A., 2007, *MNRAS*, 381, 319
 Lesaffre P., Chièze J.-P., Cabrit S., Pineau des Forêts G., 2004a, *A&A*, 427, 147
 Lesaffre P., Chièze J.-P., Cabrit S., Pineau des Forêts G., 2004b, *A&A*, 427, 157
 Lesaffre P., Gerin M., Hennebelle P., 2007, *A&A*, 469, 949
 Lesaffre P., Pineau des Forêts G., Godard B., Guillard P., Boulanger F., Falgarone E., 2013, *A&A*, 550, A106
 Levrier F., Le Petit F., Hennebelle P., Lesaffre P., Gerin M., Falgarone E., 2012, *A&A*, 544, A22
 Mignone A., Bodo G., Massaglia S., Matsakos T., Tesileanu O., Zanni C., Ferrari A., 2007, *ApJS*, 170, 228
 Monchick L., Schaefer J., 1980, *J. Chem. Phys.*, 73, 6153
 Nehmé C., Le Boulrot J., Boulanger F., Pineau des Forêts G., 2008, *A&A*, 483, 485
 Neufeld D. A., Wolfire M. G., 2017, *ApJ*, 845, 163
 Neufeld D. A., Yuan Y., 2008, *ApJ*, 678, 974
 Neufeld D. A., DeWitt C., Lesaffre P., Cabrit S., Gusdorf A., Tram L. N., Richter M., 2019, *ApJ*, 878, L18
 Pineau des Forêts G., Flower D. R., Hartquist T. W., Dalgarno A., 1986, *MNRAS*, 220, 801
 Plewa T., Müller E., 1999, *A&A*, 342, 179
 Poludnenko A. Y., Frank A., Blackman E. G., 2002, *ApJ*, 576, 832
 Reach W. T., Tram L. N., Richter M., Gusdorf A., DeWitt C., 2019, *ApJ*, 884, 81
 Santangelo G. et al., 2014, *A&A*, 569, L8
 Soubie T., 2011, *MNRAS*, 414, 350
 Soubie T., Pichon C., Kawahara H., 2011, *MNRAS*, 414, 384
 Teyssier R., 2002, *A&A*, 385, 337
 Toro E., 1999, *Riemann Solvers and Numerical Methods for Fluid Dynamics*, Vol. 10. Springer, Berlin

- Tram L. N., Lesaffre P., Cabrit S., Gusdorf A., Nhung P. T., 2018, *MNRAS*, 473, 1472
- Valdivia V., Hennebelle P., Gérin M., Lesaffre P., 2016, *A&A*, 587, A76
- Valdivia V., Godard B., Hennebelle P., Gerin M., Lesaffre P., Le Bourlot J., 2017, *A&A*, 600, A114
- Wilgenbus D., Cabrit S., Pineau des Forêts G., Flower D. R., 2000, *A&A*, 356, 1010
- Wolfire M. G., Hollenbach D., McKee C. F., Tielens A. G. G. M., Bakes E. L. O., 1995, *ApJ*, 443, 152
- Zanchet A., Godard B., Bulut N., Roncero O., Halvick P., Cernicharo J., 2013, *ApJ*, 766, 80
- Ziegler U., 2005, *A&A*, 435, 385
- Ziegler U., 2018, *A&A*, 620, A81

APPENDIX A: APPENDICES

A1 Steady-state shock validation

In order to validate our numerical method, we perform a detailed comparison between a stationary shock in CHEMSES and the result of a Paris–Durham model. We set up CHEMSES in one dimension with boundary conditions as in-flow at a speed of 2 km s^{-1} from the left and as a wall on the right, with homogeneous initial conditions. We let the simulation evolve until a steady-state shock develops, propagates leftwards and detaches from the wall by at least one full shock extent. We use twice the domain size to allow space for the shock to develop. We adopt the same viscous coefficient as for our 2D simulation set-up, but we set the chemical and thermal diffusion to zero, and adopt twice the resolution as for the the 2D set-up because these diffusion processes are absent from the Paris–Durham model.

We measure the overall compression factor $C = \rho_{\text{post}}/\rho_{\text{pre}}$ of the CHEMSES simulation to convert to the shock frame speed $u = (1 + 1/C) \times 2 \text{ km s}^{-1}$ and we find a steady-state entrance velocity of 2.04 km s^{-1} , which we adopt for the Paris–Durham code run. The positions of the temperature maxima are then matched to compare the resulting profiles. Fig. A1 shows the very good accuracy with which CHEMSES is able to recover the results of the steady-state shock code. Note that while the steady-state code runs in a few seconds on one CPU, the time-dependent problem takes 1 d on 128 cores to complete.

A2 Adiabatic shock analytical solution

Conservation of the fluxes of mass \dot{M} , momentum \dot{Q} and energy \dot{E} in a steady-state frame are expressed as

$$\dot{M} = \rho u \quad (\text{A1})$$

$$\dot{Q} = \rho u^2 + P + \varpi \quad (\text{A2})$$

$$\dot{E} = \frac{1}{2} \rho u^3 + \frac{\gamma}{\gamma - 1} P u + \varpi u \quad (\text{A3})$$

where ρ , u , P and ϖ are the mass density, velocity and thermal and viscous pressure of the fluid, ν is its viscosity coefficient (assumed constant) and γ is the adiabatic index of the ideal gas considered. The viscous pressure is expressed as

$$\varpi = -\frac{4}{3} \rho \nu \partial_x u. \quad (\text{A4})$$

We use the mass, momentum and energy fluxes to parametrize the shock model.

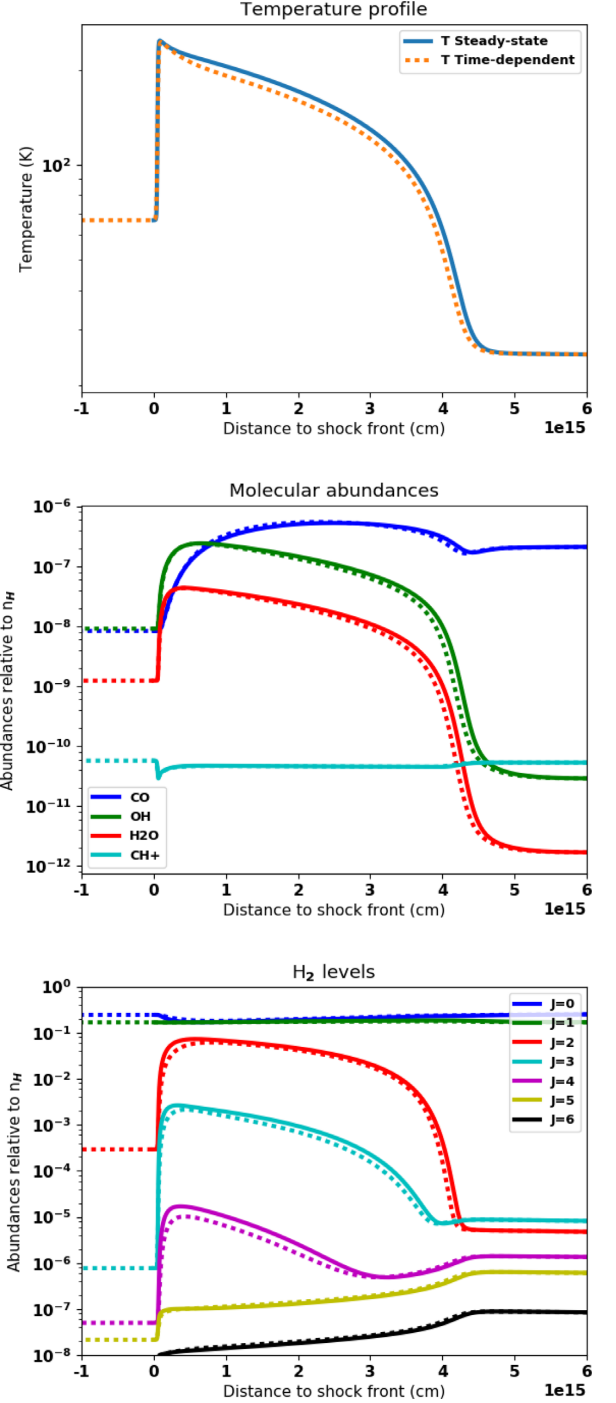


Figure A1. Validation of CHEMSES against Paris–Durham for profiles of various state variables. Solid lines show results from the Paris–Durham steady-state model, and dotted lines are for corresponding CHEMSES time-dependent results (see text).

Using equations (A1) and (A3) to eliminate variables ρ and P in equation (A2), we arrive at

$$\frac{8}{3} \frac{\nu}{\gamma + 1} \partial_x u = u^2 - 2 \frac{\gamma}{\gamma + 1} \frac{\dot{Q}}{\dot{M}} u + 2 \frac{\gamma - 1}{\gamma + 1} \frac{\dot{E}}{\dot{M}}, \quad (\text{A5})$$

which is solved as

$$u = u_{\text{mid}} - \frac{\Delta u}{2} \tanh \left[(x - x_0) \frac{3}{16} \frac{\gamma + 1}{\nu} \Delta u \right]. \quad (\text{A6})$$

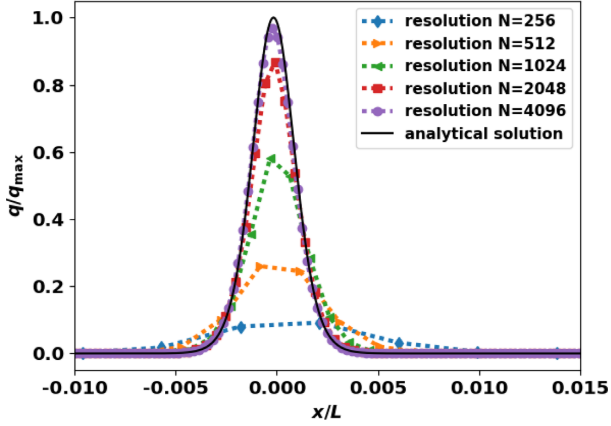


Figure A2. Physical dissipation profile (normalized to peak value) in an adiabatic ($\gamma = 5/3$) shock at Mach 1.6 with $\nu = 10^{-3}L\Delta u$ for increasing resolutions (the value given for N is the total number of pixels in the domain of size L). Note that thermal dissipation is turned off for this test: $\chi = 0$.

Here, the constants mid-velocity u_{mid} and velocity jump Δu are defined as

$$u_{\text{mid}} = \frac{\gamma \dot{Q}}{(\gamma + 1)\dot{M}} \quad (\text{A7})$$

and

$$\Delta u = \frac{2\sqrt{\Delta'}}{\gamma + 1} \quad (\text{A8})$$

with $\Delta' = \gamma^2 \dot{Q}^2 / \dot{M}^2 - 2(\gamma^2 - 1)\dot{E} / \dot{M} \geq 0$, and x_0 is simply the reference position where $u = u_{\text{mid}}$. The typical length of the shock width is therefore proportional to $\nu / \Delta u$.

Once the velocity profile is known, density and pressure can be recovered from

$$\rho = \dot{M} / u \quad (\text{A9})$$

and

$$P = (\gamma - 1) \left(\frac{\dot{E}}{u} - \dot{Q} + \frac{1}{2}\dot{M}u \right). \quad (\text{A10})$$

We can also retrieve the dissipation rate profile as $q = -\tau \partial_x u$.

A typical example is shown in Fig. 16. Note that the entrance velocity (as x tends to $-\infty$) is simply $u_0 = u_{\text{mid}} + (1/2)\Delta u$. We can then deduce the other entrance parameters using equations (A9) and (A10) with $u = u_0$.

A3 Numerical convergence for dissipation in shocks

We investigate the numerical convergence for the dissipation in an adiabatic shock at various resolutions, compared with the analytical solution just found in Appendix A2. The comparison is illustrated on Fig. A2 for various resolutions. The code we use is conservative, so the total amount of dissipation in the shock is always the same, but the fraction of dissipation that is effectively realized by the physical term increases with resolution (the remainder of the dissipation is handled by the numerical scheme). At a resolution of 1024 pixels (i.e. in the same conditions as our 2D simulation), we find that 77 per cent of the integrated dissipation is physical, with proper convergence only at 4096 zones (98 per cent). We also note that the width of the shock is already well defined at 1024 zones. Our criterion for the necessary number of pixels can hence be translated as a lower limit in the form of a Reynolds number: $N \gtrsim L\Delta u/\nu$. Note that the convergence with the number of zones is very slow: a naive test at lower resolutions could lead to a false sense of convergence. Because our scheme is second-order in both space and time, convergence is expected to be quadratic for the primary variables. However, the dissipation rate involves first-order space derivatives of the velocity, which explains why it has only linear convergence.

This paper has been typeset from a $\text{\TeX}/\text{\LaTeX}$ file prepared by the author.